HAL open science

Multi-scale statistical properties of disaggregated SMOS soil moisture products in Australia

M. Neuhauser, S. Verrier, Olivier Merlin, Beatriz Molero, C. Suere, Sylvain Mangiarotti

To cite this version:

M. Neuhauser, S. Verrier, Olivier Merlin, Beatriz Molero, C. Suere, et al.. Multi-scale statistical properties of disaggregated SMOS soil moisture products in Australia. Advances in Water Resources, 2019, 134, pp.103426. 10.1016/j.advwatres.2019.103426 . hal-02618288

HAL Id: hal-02618288

https://hal.inrae.fr/hal-02618288

Submitted on 20 Jul 2022

HAL is a multi-disciplinary open access archive for the deposit and dissemination of scientific research documents, whether they are published or not. The documents may come from teaching and research institutions in France or abroad, or from public or private research centers.

L'archive ouverte pluridisciplinaire **HAL**, est destinée au dépôt et à la diffusion de documents scientifiques de niveau recherche, publiés ou non, émanant des établissements d'enseignement et de recherche français ou étrangers, des laboratoires publics ou privés.

Distributed under a Creative Commons Attribution - NonCommercial 4.0 International License

Version of Record: https://www.sciencedirect.com/science/article/pii/S0309170819303550
Manuscript_37164388982b06fb6a87d6fd24eb2899

Multi-scale statistical properties of disaggregated SMOS soil moisture products in Australia

M. Neuhauser[1], S. Verrier, O. Merlin, B. Molero, C. Suere, S. Mangiarotti

CESBIO, Université de Toulouse, CNES, CNRS, INRA, IRD, UPS, France

Highlights

- Fractal and multifractal properties were observed on remotely sensed soil moisture products acquired from SMOS satellite (Soil Moisture and Ocean Salinity), over space scales ranging from the kilometric field scale to the continental scale
- Two scaling regimes were noticed for the soil moisture data disaggregated with DisPATCh algorithm (Disaggregation based on Physical And Theoretical scale Change), with a scaling break observed at about ten kilometers
- Fractality and multifractality were also found on remotely sensed vegetation indices and surface temperature

Abstract

Soil moisture has a strong impact on climate, hydrology and agronomy at different space scales, from the continent global scale to the local watershed. Passive microwave sensors, like SMOS satellite (Soil Moisture and Ocean Salinity), allow a global study of soil moisture on the entire globe. To have access to kilometric variability, disaggregation algorithms have been developed, such as the Disaggregation based on Physical And Theoretical scale Change (DisPATCh). This method improves the space resolution of SMOS soil moisture from 40 km to 1 km. To do this, it combines coarse-scale (≈40 km) SMOS products with fine-scale (≈1 km) optical/thermal data. Validation studies on specific scales showed the potential of DisPATCh to enhance the spatio-temporal correlation of disaggregated SM with in-situ measurements, under low-vegetated semi-arid regions. Although the efficiency of the method was revealed in these regions, no studies fully explored its statistical behavior over a continuum of space scales. In this paper, we studied and compared the spatial multi-scale statistics of the different input and output datasets involved in DisPATCh downscaling. To do this, we applied spectral and multifractal analysis on the respective products for the region of southeastern Australia, from June to December 2010. Fractal and multifractal properties (in the framework of the Universal Multifractal model) were observed on inputs of DisPATCh (SMOS soil moisture, MODIS vegetation indices and surface temperature), which confirmed and completed

[1] Corresponding author : mathis.neuhauser@cesbio.cnes.fr (M. Neuhauser)

© 2019 published by Elsevier. This manuscript is made available under the CC BY NC user license
https://creativecommons.org/licenses/by-nc/4.0/

some results reported in existing literature. For the output disaggregated soil moisture, two scaling regimes were observed, with a transition scale observed at about ten kilometers. Considering spectral analysis, at large scales (> 10 km), disaggregated soil moisture was found to have the same scaling as the original SMOS soil moisture. On finer scales (< 10 km), a different behavior was noticed, with a higher value of the slope of the power spectrum. The same scale break was detected on statistical moments, showing that both spectral and multifractal properties of DisPATCh soil moisture are characterized by this twofold scaling signature.

Keywords

Soil moisture; Multi-scale analysis; Multifractals; Disaggregation; SMOS; DisPATCh

1 Introduction

Soil moisture (SM) is a key component of the climate system and is strongly heterogeneous, at many time and space scales. Interactions between land surface and atmosphere, such as water, energy and carbon fluxes, are strongly related to SM (Ochsner et al., 2013). It has a significant role in the water cycle as it impacts runoff, infiltration and evaporation processes. Thus, SM is an important variable in several scientific fields such as hydrology (Western et al., 2004), meteorology (Dai et al., 2004), climatology (Anderson et al., 2007) and water resource management (Engman, 1991).

SM is heterogeneously distributed at different space scales, from few centimeters to several kilometers. This variability is due to environmental factors impacting directly SM at specific scale ranges (Brocca et al., 2007; Crow et al., 2012; Jana, 2010; Vereecken et al., 2014). For instance, we could mention here soil properties (texture and structure) acting at the field scale, topography features at the watershed scale, land cover (vegetation) and meteorological forcing at the regional and continental scales.

Many ground measurement techniques have been developed to acquire highly resolved SM data sets, down to centimeters in space and minutes in time (for more details see Dobriyal et al., 2012; Robinson et al., 2008; Robock et al., 2000). Although these methods are recognized as reliable and easy to implement, they are not adapted to represent spatial heterogeneity of SM at regional and continental scales (Collow et al., 2012; Crow et al., 2012).

Regional and global scale variability of SM may be acquired and studied with the help of remote sensing. Different active and passive microwave satellites allow daily measurement of surface soil moisture in the first 5 cm of the soil column (Petropoulos et al., 2015; Wigneron et al., 2003). These satellites acquire SM information thanks to the relationship between the soil dielectric constant and

water content. Active microwave sensors measure the energy reflected by the soil after sending a microwave pulse to the surface (backscatter): we find C-band Synthetic Aperture Radars (SAR) like Sentinel 1 satellite (S1) from European Space Agency (Wagner et al., 2009) and C-band scatterometers like the Advanced Scatterometer (ASCAT; Bartalis et al., 2007). These active sensors can provide space resolution from few meters (S1) to tens of kilometers (ASCAT). Their main drawback is their sensitivity to vegetation and surface roughness, which can alter useful information (SM) in the signal measured. Passive sensors, however, are less sensitive to scattering conditions. They measure the self-emission from the land surface (radiances). Good results were obtained by C- and X- band radiometers like the Advanced Microwave Scanning Radiometer-Earth observing system (AMSR-E; Njoku et al., 2003; Owe et al., 2001), or by L-band radiometers such as Soil Moisture and Ocean Salinity (SMOS; Kerr et al., 2010) and the recent Soil Moisture Active Passive (SMAP) mission (Entekhabi et al., 2010a).

L-band microwaves (1.4 GHz) have the benefit of little sensitivity to vegetation, providing optimal estimation of SM on a wider range of land cover conditions. L-band based satellite missions deliver SM products with a revisit time of 2 to 3 days. However, because of technological constraints, the spatial resolution is coarse (30-55 km), much coarser than the kilometer scale. This is a problem since hydro-agricultural applications need better resolved information, below kilometric space scales (Walker and Houser, 2004).

To address this issue, downscaling methods have been created to improve the low spatial resolution of satellite data. Downscaling algorithms are characterized by their input data (satellite products, auxiliary ground measurements, etc.) and by the type of method (physical or statistical). Peng et al. (2017) reviewed the several methods developed so far and proposed a three-group classification: satellite-based methods, methods using geo-information data and model-based methods.

The first group (I) gathers downscaling techniques which combines satellite passive microwave products with satellite highly resolved auxiliary data, such as radar or optical/thermal observations. This takes advantage of the assets of complementary remote sensing measurement techniques. Considering the fusion with high resolution radar, a change detection method was proposed by Njoku et al. (2002) to merge coarse-scale passive microwave soil moisture products and fine-scale active backscatter data. This technique consists in the linear relationship between soil moisture and backscatter data assuming the time-invariance of vegetation and surface roughness effects. The methodology was further tested in other experiments (Narayan et al., 2006; Piles et al., 2009) and proved its efficiency for improving the spatial details of soil moisture. Statistical tools were also used

to combine active and passive products, such as Bayesian merging method (Zhan et al., 2006) or wavelet-based image enhancement method (Montzka et al., 2016). This kind of approach showed the great potential of radar for improving soil moisture resolution, in particular for higher vegetation water content and different land cover types (Akbar and Moghaddam, 2015). A possible limitation of this approach is the time lag between active and passive data, due to the low revisit rate of high resolution radar. Recently, SMAP satellite was launched to bypass this problem, embedding on board one radiometer and one radar (Das et al., 2011). Unfortunately, the radar failed and no active/passive combination could be performed. However, the previous studies made to prepare the mission showed good capacity to improve spatial resolution of satellite products by merging active and passive microwave data. Another type of satellite-based method is the combination of passive microwave data with optical and thermal remote sensing data. The interest is to have the additional information of high spatial resolution and short revisit time of the optical/thermal products. The concept is to use highly resolved vegetation cover and surface temperature products to downscale coarse-scale soil moisture product. Based on the surface temperature/vegetation index triangular feature space proposed by Carlson (1994, 2007), Zhan et al. (2002) and later Chauhan et al. (2003) developed and applied this method based on a polynomial function linking high resolution SM with surface temperature, vegetation cover and surface albedo. At coarse resolution, scaling factors (regression coefficients) are estimated from this polynomial function and then used at high resolution in the same function to calculate the high resolution SM using NDVI (Normalized Difference Vegetation Index) and LST (Land Surface Temperature) obtained from the LST/NDVI feature space. An improved version was proposed by Piles et al. (2011) using brightness temperatures instead of albedo, showing better results when comparing downscaled SM with in-situ measurements. For instance, this downscaling technique was used to improve the resolution of AMSR-E soil moisture merging it with optical/thermal data measured from MODIS (Moderate resolution Imaging Spectroradiometer) (Choi and Hur, 2012) or MSG-SEVIRI (Meteosat Second Generation Enhanced Visible and Infrared Imager) (Zhao and Li, 2013). The main problem in this methodology is the non-conservativity of SM between fine-scale and coarse-scale SM. Based on the same theory, other downscaling algorithms were proposed to relate the downscaled SM with coarse observations of SM. An operationally implemented method is the downscaling algorithm DisPATCh (Disaggregation based on Physical And Theoretical scale Change; Merlin et al., 2008a; Molero et al., 2016). This algorithm is more physical because it uses soil evaporation processes to connect optical/thermal and SM data. Different applications of DisPATCh were realized to increase the ≈40 km resolution of SMOS SM to 1 km and even 100 m respectively with MODIS (Merlin et al., 2012) and Landsat-7 (Merlin et al., 2013) products. The originality of the method is the estimation of a SM proxy called Soil Evaporative Efficiency (SEE; sections 4.2 and 6.2). The latter has the advantage, compared

to land surface temperature or evapotranspiration, to be more linked to SM and to be quite constant during the day. Some improvements still need to be made about the modelling of SEE, especially on elevation and illumination effects (Malbéteau et al., 2017) or soil properties and atmospheric conditions (Merlin et al., 2016). Comparable evaporation-based methods were developed using different proxies of SM such as the Soil Wetness Index (Kim and Hogue, 2012) or the Vegetation Temperature Condition Index (Peng et al., 2016), both applied in the simple downscaling method UCLA. We can also mention algorithms directly improving the resolution of brightness temperature products (instead of retrieved SM), based on the relation between daily temperature change and daily average SM (Song et al., 2014). Generally, these downscaling methods present a significant asset considering the time coherence between the merged products, but some limitations exist. Indeed, the cloud sensitivity of optical/thermal sensors makes the application of these methods possible only under clear-sky conditions (Djamai et al., 2016).

Since SM is directly linked to geoinformation data such as topography, soil properties and vegetation attributes (Werbylo and Niemann, 2014), a second group (II) of downscaling methods were also proposed. These methods take advantage of highly resolved geoinformation data (giving information on the local attributes of the zone studied), and could give access to very high spatial resolution of SM. Topography for example was often used in downscaling approaches as an auxiliary data (Busch et al., 2012; Pellenq et al., 2003). However, certain types of geoinformation data, like soil properties, are usually provided by ground observations, which are really specific to the studied area. Thus, the application is limited to local areas and it may not be suitable for global scale study of SM.

The third class (III) of methods concerns model-based downscaling techniques. There are two types of models used here. On the one hand, there are hydrological (land surface) models. These ones are more site-specific because they try to link coarse-scale remotely sensed SM and fine-scale parameters obtained from local land surface models. The downscaling can be done through optimization techniques (Ines et al., 2013), linear regressions (Loew and Mauser, 2008) or bivariate relationships (Verhoest et al., 2015). On the other hand, there are models that analyze and describe statistics across scales: they are more generic and try to preserve statistical properties across scales. For example, Kaheil et al. (2008) proposed a wavelet-based downscaling method in order to model spatial statistical properties of fine-scale SM thanks to coarse-scale airborne SM products. Other approaches are based on the scaling (or fractal) properties of SM across spatial scales. Bindlish and Barros (2002) proposed a fractal interpolation method applied on airborne SM products, measured from Electronically Scanned Thinned Array Radiometer (ESTAR). They used power spectra to represent the fractal behavior of SM, and could improve spatial resolution from 200 m to 40 m. A few years later, Mascaro et al. (2010) applied Log-Poisson multifractal cascades on remote sensing

SM to generate simulations of fine-scale SM. The challenge here is to preserve non-stationarity from coarse to fine scales. Nevertheless, particular efforts are made to overpass this problem. For example, Kim and Barros (2002a) adapted the fractal interpolation method applying a sliding window on specific parts of the original field. They could simulate fractal variability while taking into account the local statistics of the field.

The downscaling methods of the three groups presented above have their own advantages and disadvantages, with more or less efficiency according to specific surface or climate conditions. In this study, we focus on the evaluation of multi-scale variability of SM products generated by the method DisPATCh (Merlin et al., 2008a; Molero et al., 2016). Despite its limitations related to cloud cover, this semi-physical downscaling algorithm combines low sensitivity to vegetation of L-band microwaves, high spatial resolution of optical/thermal data and it is dispensed from estimation errors commonly generated by land surface models. Several studies have been realized so far to evaluate and validate this method (Malbéteau et al., 2016; Merlin et al., 2013, 2015; Molero et al., 2016). In general, the assessment of downscaling algorithms is made comparing fine-scale output products with ground measurements. Different performance metrics are used, such as correlation, root mean square error or bias (Albergel et al., 2013; Al Bitar et al., 2012; Entekhabi, 2010b). More recently, Merlin et al. (2015) proposed a new metric that estimates the gain given by the downscaling method in terms of representativeness of downscaled data compared to non-downscaled data. To take into account scale mismatch between downscaled and ground measurements, upscaling techniques have been developed in order to bring downscaled and ground data together at common space scales (Crow et al., 2012). For example, Merlin et al. (2013) applied the DisPATCh algorithm on SMOS data while using both MODIS (Moderate resolution Imaging Spectroradiometer) and Landsat-7 auxiliary data. Coarse-scale satellite data, downscaled data and aggregated ground measurements were compared at three different scales: 40 km, 3 km and 100 m. Good results confirmed the potential of DisPATCh to improve the spatio-temporal correlation of remotely sensed SM with in-situ measurements. However, the drawback of these validation techniques is that they are restricted to specific scales. Thus, the validation of disaggregated SM products over a continuum of space scales has not been fully explored yet. Investigation of the multi-scale statistics and of possible scaling properties of these products could provide relevant information on this aspect.

During the last thirty years, several studies were carried out to describe the statistical properties of SM across spatial scales (Famiglietti et al., 2008; Rodriguez-Iturbe et al., 1995). Different analytical methods were proposed. The most commonly used are spectral-wavelet analysis (Si, 2008) and multifractal analysis (Kim and Barros, 2002b; Mascaro et al., 2010; Oldak et al., 2002). In 1995, Rodriguez-Iturbe et al. highlighted for the first time the fractal behavior of SM from remote sensing:

the spatial variance of SM followed a power law decay as a function of aggregation scales ranging from 30 m to 1 km (Washita Experiment 1992, USA). Later studies showed that such a scaling behavior of SM variance could be extended to wider range of scales: up to regional scale (Hu et al., 1997) and even to continental scales (Rötzer et al., 2015). Similar research works demonstrated that increasing area extent (increasing size of the total area) induced the increase of SM variance according to a power law function (Famiglietti et al., 2008; Rötzer et al., 2015; Brocca et al., 2012). Moreover, in Oldak et al. (2002), the fractal scaling of SM was revealed to be multifractal: the power law was also applicable to the first six statistical moments of airborne SM products for scales ranging from hundreds of meters to tens of kilometers (Washita'92 Experiment and Southern Great Plains Experiment 1997, USA). Multifractal scaling was then detected in SM fields (Das and Mohanty, 2006; Kim and Barros, 2002b; Lovejoy et al., 2008; Mascaro et al., 2010). Since SM variability is directly related to the amount of soil wetness (Brocca et al., 2007; Famiglietti et al., 2008), it may be expected that scaling properties of SM may vary according to the state of SM. Indeed, when plotting SM variance power law in log-log coordinates, Rodriguez-Iturbe et al. (1995) and Manfreda et al. (2007) found that the corresponding slope of the curve was increased during drier periods, revealing seasonal variations of SM scaling (Rötzer et al., 2015). Moreover, it was observed that SM variability was not governed by a single scaling behavior, but by different scaling regimes depending on the range of scales. At the field scale, SM variability is mainly related to land surface characteristics such as soil properties or topography, whereas at larger scales it is impacted by meteorological quantities like rainfall or evapotranspiration (Cayan and Georgakakos, 1995; Entin et al. 2000). Studies based on semi-variograms (Ryu and Famiglietti, 2006; Korres et al., 2015) and spectral/moments analysis (Kim and Barros, 2002b) revealed the presence of scale breaks closed to this transition scale between land surface and meteorological regimes. Though, the aforementioned characteristics of SM highlight its complexity and its high degree of nonlinearity due to hydrometeorological processes acting at different space scales, attesting the necessity to better understand the scaling behavior of SM for applications such as data assimilation or downscaling (Rötzer et al., 2015).

In this paper, we propose an alternative and complementary method for verifying the multiscaling behavior of DisPATCh products. To do this, we studied and compared the statistical spatial properties across scales of the downscaled SM, the original SMOS SM and the MODIS auxiliary data, by applying spectral and multifractal analysis in the framework of the Universal Multifractal (UM) model (Schertzer and Lovejoy, 1987). The definition of multifractal formalism is given in section 2, with a particular attention paid to UM parametrization. The methodology followed for multifractal (and spectral) analysis is detailed in section 3. Section 4 describes the case study and the data set. Then, the different results obtained from spectral and multifractal analysis are presented in section

5. Finally, section 6 proposes explanations to the multiscaling behaviors of DisPATCh SM, and a general conclusion of this study is given in section 7.

2 Theory of multifractals

During the last century, several studies showed that many geophysical processes could present scale invariance properties. This was first anticipated by Richardson (1922) in the case of turbulence: he described turbulent flows as cascade processes that transfer kinetic energy from large to small scales. Based on this approach, statistical models of turbulence were proposed such as the famous Kolmogorov law (1941) to describe velocity increments. Later research works generalized the study to take into account the heterogeneity of the energy flux (Kolmogorov, 1962; Obukhov, 1962; Yaglom, 1966). Multi-scale models such as multiplicative cascades were therefore proposed to reproduce scale invariance properties through the use of fractal geometry. Later, scale invariance was noticed in other geophysical fields: in his study of the coast of Britain, Mandelbrot (1967) revealed the presence of fractal properties in topography.

2.1 From fractal sets to multifractal fields

The concept of fractal dimension has been used in many works related to multi-scale analysis and geophysical modelling. Indeed, the term “fractal” refers to any entity (time series or 2D/3D random field) in which each part presents similar properties, geometrically or statistically, to the ensemble. In this manner, the structure of a fractal entity is characterized by scale invariance. Initially, the notion of fractal was introduced in the late 19th century in geometry with the creation of sets, i.e. mathematical objects, having unusual properties, especially a non-integer Hausdorff dimension, called later by Mandelbrot as “fractal dimension” (Mandelbrot, 1967). Scale invariance, in the statistical sense, was theoretically proposed by Kolmogorov in 1940 with the introduction of the fractional Brownian motion. This model could generate random time series whose trajectories present fractal properties in terms of statistical distribution. It illustrates the physical interest of fractal random processes, since Brownian motions are somewhat ubiquitous in physics. Mandelbrot and Van Ness (1968) made it famous by introducing it to more physical models. In particular, the first fractal stochastic models of topography were developed based on this theory (Mandelbrot, 1975).

These stochastic models aim to represent the simple scaling (monofractal) behavior of geophysical processes. In this context, the fractal dimension or scaling parameter is assumed to be unique, restricting multi-scale modelling to a specific class of variability. However, most geophysical processes are characterized by more complex statistics. In case of operational hydrology, rare and extreme events, present in precipitation or soil moisture for example, correspond to high order

statistics and need to be detected (Hubert et al., 1993). Therefore, multifractal models, characterized by an infinite spectrum of fractal dimensions, have been proposed to account for a more exhaustive set of statistics. Schertzer and Lovejoy (1987), based on the findings of Parisi and Frisch (1985), initially established the multifractal formalism through the fundamental equation:

$$Pr(\phi_\lambda > \lambda^\gamma) \approx \lambda^{-c(\gamma)} \tag{1}$$

where ϕ_λ is a positive normalized random scalar process, time series or random field defined on R^2 or R^3. The mean of the process is assumed to be statistically conserved across scales. λ is the observation resolution, here defined as the inverse of the scale that can be seen as the sampling time or pixel size for time and space domain processes respectively and $\approx$ indicates an equality within the limits of slowly varying functions. Eq.1 expresses the fact that for a multifractal process, the probability of exceeding a threshold varies as a power law of the resolution with exponent $c(\gamma)$. This exponent is called as fractal codimension of the process, depending on the amplitude of thresholds. The thresholds are defined by the following power law:

$$T_\lambda = \lambda^\gamma \tag{2}$$

with γ the notion of singularity, characterizing the amplitude of the process independently of the scale. Each singularity is associated to a fractal codimension $c(\gamma)$, corresponding to a family of thresholds of various amplitudes. From a more physical point of view, high singularities (detected by high thresholds) are related to rare and extreme events, with high fractal codimensions and inversely low (box-counting) fractal dimensions D_f (Mandelbrot, 1967). Indeed, the latter are related to the dimension of space D through the relation $c(\gamma) = D - D_f$. Therefore, $c(\gamma)$ can be described as a codimension function, increasing with γ, which completely characterizes the multi-scale statistical properties of the field ϕ_λ. In general, if the field is multifractal, $c(\gamma)$ is found to be convex and positive (with a fixed point C_1 imposed by the condition of canonical conservation), whereas monofractality is associated to the trivial case $c(\gamma) = const.$

Since probability distributions and statistical moments are related by a Mellin transform, Schertzer and Lovejoy (1987) proposed an equivalent equation to (1):

$$\langle \phi_\lambda^q \rangle \approx \lambda^{K(q)} \tag{3}$$

where $\langle\cdot\rangle$ is the statistical averaging operator, q is the order of the moment ($q \geq 0$), and $K(q)$ is the moment scaling function. Eq.3 expresses that, for any fixed moment order, statistical moments and resolution are linked through a power law. Singularities and moment orders are directly linked, since the moment scaling function $K(q)$ is the Legendre transform of the codimension function $c(\gamma)$.

Similarly to $c(\gamma)$, $K(q)$ is a convex function (with the special case $K(1) = 0$ related to the conservation of the mean across scales), which entirely characterizes the multifractal field.

2.2 Multiplicative cascades

Multiplicative cascades are stochastic models that can be used to build multifractal fields. Cascades are multiplicative processes because they are defined by an iterative multiplicative construction: considering a two dimensional random signal (field), each pixel at resolution λ_{n+1} (with n the construction level of the cascade) is the product of the embedding pixel at coarser resolution (λ_n) multiplied by a random variable $\mu\varepsilon$. This is described by the following equation:

$$\phi_{\lambda_{n+1}} = \mu\varepsilon \times \phi_{\lambda_n} \tag{4}$$

In this manner, the statistical properties of the field $\phi_{\lambda_{n+1}}$ are directly related to the statistical properties of the coarser field ϕ_{λ_n}. If all the multiplicative random variables used for each step of the iterative construction are independent and identically distributed, and distributed independently of the scale, the final field presents scale invariant properties.

Several models of cascades have been developed so far. First models were built within the framework of turbulence, such as the α-model (Schertzer and Lovejoy, 1984) which corresponds to discrete construction of cascades: the multiplicative random variables are limited to two possible fixed values, respectively leading to increasing or decreasing pixel value when the resolution is refined. Later, more elaborated models were constructed generalizing the discrete case to continuous cascades (Dubrulle, 1994; Schertzer and Lovejoy, 1987, 1991, 1997; She and Levêque, 1994). The latter are based on an infinite number of steps between any pair of resolutions, leading to continuity in scale. The benefit of continuous cascades is twofold. First, they can represent possibly more realistic structures by avoiding any arbitrary discretization of scales. Moreover, they often converge toward random processes which are characterized by a small number of degrees of freedom (special cases of log-infinitely divisible distributions). This is interesting considering that multifractal fields built by multiplicative cascade processes would otherwise need an infinite number of scaling parameters (one for each fractal dimension). For example, She and Levêque (1994) proposed a continuous cascade model based on Log-Poisson statistics, and Schertzer and Lovejoy (1987) used Log-stable random variables to build the Universal Multifractal model. In both models, only two fundamental parameters are needed to fully define multifractality.

2.3 Universal Multifractals

Physically, multifractal fields built by Log-Poisson or Log-stable cascades have a high degree of generality in geophysics. Log-Poisson model has been successfully applied to different geophysical

variables such as rain (Deidda, 2000), or even soil moisture (Mascaro et al., 2010). However, this model can have disadvantages of representing a restricted range of variabilities, which may make it unsuitable for modeling processes with unbounded singularities. On the other hand, by assuming the stability of the random variables and suitable renormalization, UM model is likely adapted for characterizing a wide range of processes: topography (Lavallée et al., 1993), rain and clouds (Tessier et al., 1993) and more recently soil moisture and vegetation optical indexes (Lovejoy et al., 2008). Moreover, a possibly more immediate physical interpretation of the parameters is found in this model. For mathematical and physical arguments supporting the universality of UM model, see Schertzer and Lovejoy (1997); see also Gupta and Waymire (1997) for discussion about its generality. UM model defines the moment scaling function using two "universal" parameters, through the following equation (Schertzer and Lovejoy, 1987):

$$K(q) = \frac{C_1}{(\alpha-1)}(q^{\alpha} - q) \tag{5}$$

where α is the degree of multifractality of the field. It varies between 0 (monofractality) and 2 (log-normality) and expresses how fast the codimension evolves as a function of the singularity. The second parameter C_1 is the codimension giving the dominant contribution to the mean value of the field (related to moment of order 1): $C_1 = K'(1)$. Physically, it indicates inhomogeneity (dispersion) of the field: it varies from 0 (homogeneous field) to the dimension D of the embedding space (very intermittent field). Because of Legendre transform, $c(C_1) = K'(1)$ is also defined as the fixed point of the codimension function.

2.4 FIF model

Generally, most of the geophysical fields are non-conservative, i.e. integrated processes defined by a certain degree of fractional integration. This appellation comes from multifractal cascade models: see Gagnon et al., 2006 for detailed explanations on this formalism. Thus, to account for a wider range of processes, an extension of the UM model to non-conservative fields has been proposed (Schertzer and Lovejoy, 1991): the Fractionally Integrated Flux (FIF) model. It expresses the degree of fractional integration of the UM field, using a third parameter *H*. The latter is called the order of integration and defines the non-conservativity of the field: in plain words, the larger is *H*, the smoother is the field. The integrated flux is noted R_λ and is characterized by a power law variation of its stationary increments:

$$\Delta R_\lambda \approx \phi_\lambda \, \Delta x^H \tag{6}$$

where ΔR_λ are the increments (fluctuations of the flux) estimated over a varying window Δx, which is equivalent to the space scale *l*. Note that when *H = 0*, the equation corresponds to the

conservative case ϕ_λ. Additionally, in the case of two dimensional fluxes, Eq.6 also applies for other directions (i.e. Δy increments), with the same exponent *H* if the process is isotropic.

Hereafter in this article, the appellation proposed in Lovejoy and Schertzer (2010) will be followed: non-integrated cascades will be called conservative fluxes, due to the conservation of the mean, and fractionally integrated "non-conservative" processes will be called "random fields" or simply "fields".

3 Multifractal analysis methodology

The different techniques used to analyze the multi-scale properties of DisPATCh related products are detailed in this section. The methodology is based on the multifractal theory presented in the precedent section. Because our study treats only satellite images, we will focus on the two dimensional versions of these techniques.

3.1 Power spectrum: preliminary evidence of scaling

Spectral analysis is a methodology often used in geophysics to characterize, in an easy and rapid way, some scaling properties of fields over different space scales (Lovejoy et al., 2008). Thanks to its high sensitivity to scale breaks, scaling regimes can be easily identified. In a first step, the two-dimensional power spectral density $P(k_x, k_y)$ of the data under analysis, X, is estimated:

$$P(k_x, k_y) = |fft(X)|^2 \tag{7}$$

with *P* the power spectral density defined on both vertical and horizontal image axis, corresponding respectively to k_x and k_y wavenumbers (spatial frequencies). Here, the estimation of the PSD is done through a two-dimensional *fft* or Fast Fourier Transform. Then, the one dimensional isotropic angle-integrated power spectrum $E(k)$ is obtained (Lovejoy et al., 2008; §8):

$$E(k) = \int_{\|\vec{k}\|=k} P(\vec{k}) d\vec{k} \tag{8}$$

where *k* is the modulus of the wavenumber and $\|.\|$ is the Euclidean norm. Since it expresses space frequencies, *k* is directly related to the space resolution λ. If the process presents scaling properties, the spectrum should follow a power law, where β is the negative slope of $E(k)$ on a log-log graph:

$$E(k) \approx k^{-\beta} \tag{9}$$

β is called the spectral exponent and is directly related to the FIF parameters through the equation:

$$\beta = 1 + 2H - K(2) \tag{10}$$

In this manner, β also gives first indications about the possible conservative nature of the field, since integrated flux ($H > 0$) should correspond to spectral exponent greater than 1. Note that power spectrum is a second-order statistic, hence the term $K(2)$.

3.2 Statistical moments: multifractal properties

To test the presence of multifractal properties in the data (Eq.3), statistical moments and moment scaling function need to be estimated. To do this, different steps must be followed. First, the underlying conservative field $\oplus_{\lambda_{max}}$ has to be reconstructed from the data, at the maximum observation resolution λ_{max}. Because the possible existence of a fractional integration of order H (Eq.6), a fractional derivative of the same order should be done. In this study, the modulus of the gradient was applied to the data. Indeed, this operator provides a simple and good numerical approximation of the fractional derivation without prior knowledge of *H* order (Lavallée et al., 1993):

$$\oplus_{\lambda_{max}} = \sqrt{\left(\frac{\partial R_{\lambda_{max}}}{\partial x}\right)^2 + \left(\frac{\partial R_{\lambda_{max}}}{\partial y}\right)^2} \tag{11}$$

Once the conservative field is retrieved, $\oplus_{\lambda_{max}}$ is normalized by its mean.

The second step involves the degradation of the field at lower resolutions $\lambda < \lambda_{max}$. It aims to approximate the inversion of the stochastic multiplicative cascade by iteratively averaging the field at coarser scales: each coarse pixel (level *n* of the cascade) is obtained by a simple average of neighboring finer pixels (level *n+1*). Note that each roughened pixel size is a power of two multiplied greater than the observation scale l_{min} ($= {\lambda_{max}}^{-1}$).

Finally, empirical moments (i.e. computing *q*-th order moments in Eq.3 while replacing statistical averages by empirical averages) are then computed for various orders and resolutions. On a log-log graph, the different moments are plotted as a function of the resolution. If linearity is observed for each moment curve, at least over a significant range of resolutions, Eq.3 is therefore verified, which is the signature of multifractality. The empirical moment scaling function can be estimated, with $K(q)$ corresponding to each linear fit of *q*th order moment. Afterwards, the universal parameters α and C_1 may be obtained by optimization according to the UM model form of $K(q)$ (Eq.5).

3.3 Structure functions: some evidence of non-conservativity

A convenient way to reveal the non-conservative/fractionally integrated nature of the integrated flux R_λ (Eq.6), is to compute its first order structure function:

$$\Delta R_\lambda(\Delta x) = \langle |R_\lambda(x + \Delta x) - R_\lambda(x)| \rangle \tag{12}$$

If the flux is indeed non-conservative, the order of integration H should be the slope of the increments ΔR_λ, plotted in a log-log graph as a function of space scale Δx. This technique will be used in this study to estimate the H parameter.

4 Case study and data

4.1 C4DIS processor and satellites products

The different products analyzed in this study are input and output data of C4DIS (CATDS level-4 DISaggregation) processor (Molero et al., 2016). This processor includes the first operational version of the DisPATCh algorithm, taking into account the best configurations according to the latest studies (Merlin et al., 2010a, 2010b, 2013). Because the algorithm is still evolving, C4DIS products are called as "scientific" (Molero et al., 2016): users can have access on demand to the products over specific areas of the world.

As presented earlier, the downscaling method combines SMOS microwave data and MODIS optical/thermal data. The SM data is given by the SMOS Level-3 daily global SM product (reference: MIR CLF31A/D). This product is provided by the Centre Aval de Traitement des Données SMOS (CATDS), which is the French ground segment for SMOS Level-3 and Level-4 products. The SM data is acquired every day at a radiometric resolution that varies between 35 and 55 km, 40 km in average, from L-band brightness temperature measurements (Kerr et al., 2012; Wigneron et al., 2007). SMOS Level-3 products are delivered on the EASE (Equal Area Scalable Earth) grid, with a grid spacing of 25 km × 25 km.

The optical/thermal products come from the MODIS sensor, embedded on both Aqua and Terra satellites. Two types of auxiliary data are used in DisPATCh. First, there is Land Surface Temperature (LST). It is extracted from the MODIS Level-3 daily products: MYD11A1 (Aqua) and MOD11A1 (Terra). These temperature products are estimated from thermal infrared radiances emitted from the surface (3-15 µm). Then, the second auxiliary data is Normalized Difference Vegetation Index (NDVI), given by the Level-3 16-day Terra product (MOD13A2). The vegetation index is computed from surface reflectances in red (0.7 µm) and near infrared (0.8 µm) wavelengths. Both LST and NDVI products are provided at 1 km resolution by the NASA Land Processes Distributed Active Archive Center (LP DAAC). They are presented on a sinusoidal grid, with a grid spacing slightly smaller than kilometer: 0.93 km × 0.93 km (Solano, 2010; Wan, 2006). We may notice that LST products have daily time resolution, whereas NDVI products are representative of a period of 16 days.

Output DisPATCh products are generated every day by the C4DIS processor. Their resolution is that of MODIS products (1 km), and they are presented on an equal-spaced lat-lon WGS84 grid, with

a grid spacing of 0.01° (≈1.12 km). For simplicity, in the following we'll make the approximation 0.01° = 1 km. One single downscaled image is the result of the combination of four downsampled SMOS SM images, one MODIS NDVI image, and up to six MODIS LST images corresponding to 3 consecutive days of Aqua and Terra acquisitions (for more details on the combination methodology see Malbéteau et al., 2016; Merlin et al., 2012; Molero et al., 2016). In other words, in the final product, each high resolution output pixel comes from the average of 24 possible disaggregated pixels (up to 24 SM-LST possible pairs). The advantage of this composition is that uncertainty in downscaled SM can be potentially reduced and estimated, and time-coverage is improved (Malbéteau et al., 2016).

4.2 DisPATCh algorithm

DisPATCh is based on a semi-empirical model that estimates the Soil Evaporative Efficiency (SEE) from high resolution (HR = 1 km) LST and NDVI products. The method is based on the separation of MODIS LST into its soil and vegetation components, respectively referred in this study as $T_{s,HR}$ and $T_{v,HR}$. To do this, the approach relies on a variant of the trapezoid method from Moran et al. (1994) which interprets the feature space defined by MODIS LST and NDVI-derived fractional vegetation cover $f_{v,HR}$. The purpose here is to extract the soil temperature $T_{s,HR}$ according to the following equations:

$$T_{s,HR} = (LST - f_{v,HR} * T_{v,HR})/(1 - f_{v,HR}) \quad (13)$$

$$\text{with } f_{v,HR} = (NDVI - NDVI_{soil})/(NDVI_{veget} - NDVI_{soil}) \quad (14)$$

In equation 13, the vegetation temperature $T_{v,HR}$ is calculated according to Moran et al. (1994). $NDVI_{soil}$ and $NDVI_{veget}$ in (14) are respectively the NDVI obtained from bare soil (set to 0.15) and from full-cover vegetation (set to 0.90).

Then, MODIS-derived soil temperature $T_{s,HR}$ allows to estimate SEE_{HR} at 1 km resolution following the methodology proposed by Merlin et al. (2012):

$$SEE_{HR} = (T_{s,max} - T_{s,HR})/(T_{s,max} - T_{s,min}) \quad (15)$$

where $T_{s,max}$ and $T_{s,min}$ are endmembers estimated from the approximations of Merlin et al. (2013) considering the relations between the minimum/maximum of LST and the associated $f_{v,HR}$ (more details can be found on these estimates in Molero et al., 2016; p.4).

SEE is used to describe the spatial variability of SM within the low resolution (LR = 40 km) pixel given by SMOS product. High resolution SM (SM_{HR}) is linked to high resolution SEE (SEE_{HR}) through the linear model proposed by Budyko (1956) and Manabe (1969):

$$SEE_{HR} = \frac{SM_{HR}}{SM_p} \quad (16)$$

where SM_p is a LR parameter depending on atmospheric conditions and soil properties. In the C4DIS processor, this parameter is computed at low resolution at each execution from daily SMOS SM (SM_{LR}) and SEE averaged inside the LR pixel (SEE_{LR}):

$$SM_p = \frac{SM_{LR}}{SEE_{LR}} \quad (17)$$

The disaggregation is finally realized by applying a first order Taylor expansion to the SEE and SM dataset. The downscaling relationship is written as:

$$SM_{HR} = SM_{LR} + SM'(SEE_{LR}) \times (SEE_{HR} - SEE_{LR}) \quad (18)$$

with $SM'(SEE_{LR})$ the partial derivative of SM relative to SEE computed at low resolution. Here, this derivative simply equals the SM_p parameter estimated according to (17).

4.3 Study area

Australia is a wide country, with an area of almost 8 million km² and characterized by various surface and climate conditions. Thus, it is a suitable area to study spatial variations of soil moisture over a wide range of scales. Many studies on SM have been carried out in Australia in order to monitor SM variability using ground, airborne and satellites data (Smith et al., 2012). Among others, we can mention the National Airborne Field Experiment 2006 (NAFE'06; Merlin et al.., 2008b) and the Australian Airborne Calibration/validation Experiments for SMOS (AACES; Peischl et al., 2012). These experiments were realized over the Murrumbidgee catchment (82 000 km², Fig.1), located at the southeastern part of Australia. Because of its variable climatic conditions (humid in the east, semi-arid in the west), this region was used for validating satellites missions such as SMAP (Panciera et al., 2014) or SMOS. SM products delivered by SMOS were assessed during the AACES experiments, which took place in 2010 over two periods: January-February (AACES-1) and September (AACES-2). Wide spatially distributed networks of in-situ measurements (OzNet hydrological monitoring network; Smith et al., 2012) and transect flights (Polarimetric L-band Multibeam Radiometer; Peischl et al., 2012) were used to validate SMOS data. In this context, benefiting from a dense SM dataset at different space scales, some of the first applications of DisPATCh algorithm were realized during the AACES experiments (Merlin et al., 2012). These works showed the efficiency of DisPATCh under low-vegetated semi-arid areas, and its potential to evaluate coarse-scale SMOS products. Later studies (Malbéteau et al., 2016; Molero et al., 2016) continued the evaluation and improvement of DisPATCh algorithm over the Murrumbidgee catchment.

In this paper, DisPATCh analysis is made during the 7-month period from June to December 2010, taking advantage of previous DisPATCh studies over this period. We choose to extend the study area, from the Murrumbidgee catchment to the Murray Darling Basin (MDB, 1 million km², Fig.1). The first reason of this choice is related to the main objective of the study, which is the analysis of DisPATCh related products over different space scales. Though, our study covers a large range of scales, from the pixel size (kilometer scale) to the full basin extent (1300 ×1400 km²), giving a new point of view considering DisPATCh validation. Moreover, spectral and multifractal tools presented in section 3 cannot be properly applied if the data size is not sufficient enough. Because of its low resolution, it would be inappropriate to do multiscale analysis of SMOS SM over the Murrumbidgee catchment ("images" would be smaller than 5 × 5 pixels).

MDB is located in southeastern Australia and contains more than 20 catchments such as Murrumbidgee in its south part (Fig.1) The climate is sub-tropical in the North-East (average annual precipitation up to 1500 mm), semi-arid in the West (average annual precipitation less than 300 mm) and mostly temperate in the South (snowfall during winter on the peaks of the Great Dividing Range). Regarding to land use, West is made of wide plains essentially composed of saltbush shrublands and mulga lands. From South to North-East, there are the mountains of the Great Dividing Range reaching 2 300 m in altitude. Irrigation, dry land cropping and pastures are spread over the basin, but most of the irrigated areas are located in the South (like Murrumbidgee region).

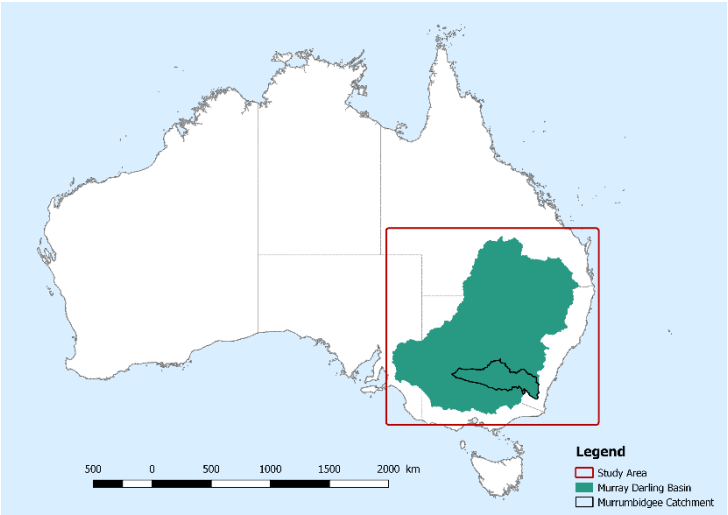

Figure 1. The study area includes the Murray Darling Basin (1 million km²), southeastern Australia.

4.4 Data preprocessing

Before applying the multi-scale analysis, preprocessing must be done on the different satellite products. The first preprocessing step is to handle the missing values. Because of technology or acquisition conditions, all satellite sensors provide products that present more or less missing values. These can be caused by failures in the data acquisition or delivering, or even voluntarily generated by the production center when discarding incorrect values. In our case, SMOS products can be affected by unauthorized emissions that cause radio frequency interference (RFI). SMOS SM used in this study are pre-filtered by CATDS in order to remove pixels with more than 10% RFI probability (Kerr et al., 2013; Olivia et al., 2012). Considering MODIS products, cloud pixels are also removed to avoid the impact of atmosphere on downscaled data. Though, missing values in output DisPATCh products are mainly caused by the accumulation of missing values coming from inputs. Thanks to the 24 averaged HR outputs combination implemented in C4DIS processor (section 4.1), the probability to get missing values in the final averaged downscaled product is reduced. In our study, we applied bilinear interpolation in each satellite image to fill in missing data (noted NaN). To do this properly, some conditions were established. To minimize the impact of data interpolation on spectral and multifractal analysis, each image with more than 40% of NaN were discarded. Moreover, in order to treat separately land-surface NaN values from sea areas located outside the continent, the latter were filled with zeros. Previous studies showed that biased multifractal parameters could be obtained from data containing significant proportion of zeros (De Montera et al., 2009; Verrier et al., 2010, 2011). Thus, we made sure to select images whose ground area contains a minimum of sea pixels (less than 10 %).

In a second stage, sub-images of $2^n \times 2^n$ pixels need to be selected over the MDB area. To estimate statistical moments over different spatial resolutions, images must indeed be square, with a number of pixels equal to a power of two along each dimension (section 3). Because of different satellites projection grids and spatial resolutions, selected sub-images from different satellites do not cover exactly the same area and they do not completely match to the original MDB area. Figure 2 presents examples of sub-images obtained for DisPATCh SM, SMOS SM and MODIS NDVI, whose size is respectively 1024 × 1024, 64 × 64 and 1024 × 1024 pixels (for readability, during preprocessing all MODIS products were projected from sinusoidal to orthogonal lat/lon coordinates; Sohrabinia, 2012). Considering the different grid spacing of the products and sub-images size condition, the sub-image selected for SMOS SM covers the entire MDB (1600 × 1600 km²), whereas the sub-images selected for DisPATCh and MODIS products are smaller (around 1000 × 1000 km²). It is important to notice that, while they have similar spatial resolution and a same number of pixels, DisPATCh SM and MODIS images do not exactly correspond to the same ground area. This is caused by slightly different

grid spacing for the two products, 1 km for DisPATCh and 0.93 km for MODIS (Solano, 2010; Wan, 2006). For simplicity, we'll consider in the following that both DisPATCh and MODIS products present

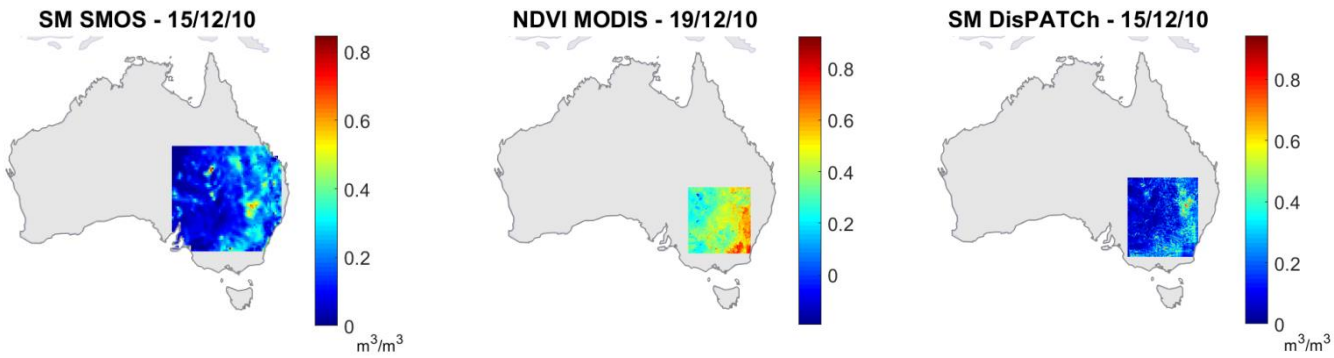

Figure 2. Sub-images selected for each satellite product over the Murray Darling Basin.

a grid spacing of around 1 km.

Table.1 summarizes the main characteristics of our preprocessed satellite dataset. Two important observations should be highlighted. First, considering their daily revisit time, few DisPATCh SM and MODIS LST images are retained over the full June-December period: only 12 maps for DisPATCh and around 70 maps for MODIS LST. This is directly related to the significant number of missing values that is in average 30 % in these two types of products. Therefore, missing values in downscaled SM seem to be mostly generated by those in LST products, probably due to the presence of clouds in the data. Then, another point concerns the different surface areas of the preprocessed products. Because they do not fully overlap, SMOS and DisPATCh sub-images may capture different SM dynamics. Extreme events occurring in northern MDB are observed in SMOS data whereas it may not be taken into account in DisPATCh data. However, we ensured that all products did have the widest area in common, focusing on irrigated regions in the middle-south part of the basin (like Murrumbidgee).

PRODUCTS	Revisit (day)	Effective resolution (km)	Grid spacing (km)	Surface area (km^2)	Number of images (with NaN% < 40%)	Average NaN rate (%)
SM DISPATCH	1	1	1	1024 x 1024	12	32
SM SMOS	1	40	25	1600 x 1600	203	3
LST Aqua-MODIS	1	1	≈ 1	950 x 950	60	28
LST Terra-MODIS	1	1	≈ 1	950 x 950	82	26
NDVI Terra- MODIS	16	1	≈ 1	950 x 950	13	10

Table 1. Main characteristics of satellites products analyzed in this study. We also mentioned the surface area, the number of images conserved, and the average rate of missing values (without sea areas) of the dataset after preprocessing.

5 Results

5.1 Spatial power spectra

Figure 3 shows the mean power spectra estimated over the full period (June-December 2010) of the different input and output products involved in DisPATCh (it represents an average spectrum based on individual spectra obtained within the period). Each spectrum is plotted in log-log coordinates, with horizontal axis converted into space scale l $(= k^{-1})$, expressed in kilometers. Considering SMOS SM and MODIS products, the mean spectra are found to be scaling over the entire range of scales. This is observed by a linear evolution of $log(E(k))$ (Eq.9), with coefficients of determination R^2 greater than 0.9 for each spectrum (Table.2). Note that R^2 is used as a measure of the goodness-of-scaling, estimated from the linear regression between $log(E(k))$ and $log(l)$. However, a different behavior is noticed for the disaggregated SM spectrum. Two scale ranges seem to appear, with an increasing slope on scales lower than about ten kilometers. A segmentation algorithm was applied on this spectrum (D'Errico, 2017), which confirmed a scale break at $l \approx 10$ km. According to the different values of spectral slopes obtained (Table.2), a three-group classification was proposed:

- <u>β ≈ 1</u>: *SMOS SM, MODIS vegetation index and disaggregated SM (l > 10 km)*
  For these three products, the negative slope is found to be close to one. Though, according to Eq.10, this may reveal the conservative nature of the fields ($H \approx 0$). Moreover, these values are quite similar to the estimates proposed in literature: Lovejoy et al. (2008) found β = 1.2 for both vegetation and soil moisture indexes (from MODIS products, Guadalajara, central Spain, July 2006). Previous studies on topography, especially on volcanic surfaces (Laferrière and Gaonac'h, 1999), found comparable results with quite low degree of fractional integration. Since topography can affect the spatial distribution of SM and vegetation (Kim and Barros, 2002b), it is not surprising to observe similar scaling behavior between these fields.
- <u>1 < β < 2</u>: *MODIS surface temperature (from both Aqua and Terra satellites)*
  LST spectra have β values greater than 1. Here, surface temperature seems to correspond to a non-conservative field ($H > 0$). These spectral slopes may be comparable to those obtained in literature on precipitation fields (Lovejoy and Schertzer, 2008), showing possible connections between the spatial distribution of surface temperature and that of rainfall, and therefore with the underlying (turbulent) atmospheric dynamic (Schmitt et al., 1993).
- <u>β > 2</u>: *disaggregated SM (l < 10 km)*
  On small scales, DisPATCh SM spectrum presents a relatively large slope, reflecting a high degree of fractional integration ($H > 0.5$). To our knowledge, such high value of spectral exponent has

never been observed in previous studies on SM fields. However, comparable scaling was obtained on SM time series, revealing spectral slopes greater than 2 (Katul et al., 2007).

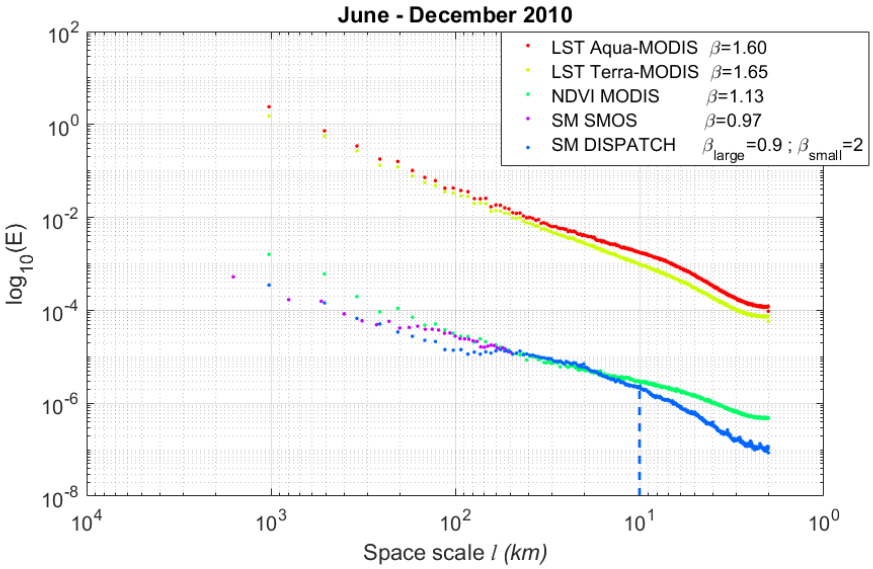

Figure 3. Mean angle-integrated power spectra of DisPATCh related products (over the full June-December period). β_{large} and β_{small} refer to disaggregated SM spectral exponents obtained respectively from scales l > 10 km and scales l < 10 km.

From these spectral observations, a similar scaling seems to appear between the original SMOS SM and the disaggregated SM on scales greater than 10 km, but this behavior is found to change for scales lower than about ten kilometers. A comment may also be made on LST power spectra and their linear regressions : although R^2 coefficients present good values on the entire range of scales (> 0.9), a scale break may be observed at about the same spatial scale found for DisPATCh spectrum ($l \approx 10$ km). The scale break seems less pronounced but it could be related to that of DisPATCh. This point will be discussed in section 6.2.

This twofold scaling regime of DisPATCh SM can be also observed on each specific date of the study period (with R^2 coefficients greater than 0.9 on almost all images and on both scale ranges). Figure 4a shows the time series of the individual spectral exponents estimated for all products (i.e. spectra computed for each image). From June to December, a significant difference of β values is observed between the two scale ranges of disaggregated SM. For example, on July 9 (Fig.4b), power spectra are found to be similar as mean ones presented above (Fig.3). In particular, the same scale break is still observed for disaggregated SM at about ten kilometers. Another remark concerns the amplitude of the scale break according to seasons. Figure 4a shows that, for disaggregated SM, the difference between the spectral exponents of small scales and large scales (respectively blue triangle and blue star symbols) is more important during the last three months of the period. At small scales, the spectral slope suffers a drastic change from around 1.9 (Jun-Jul-Aug-Sept) to 2.3 (Oct-Nov-Dec,

i.e. spring and early summer in Australia). The amplitude of the scale break observed in DisPATCh SM could be related to the seasonal conditions of the study area. This will be discussed in section 6.1.

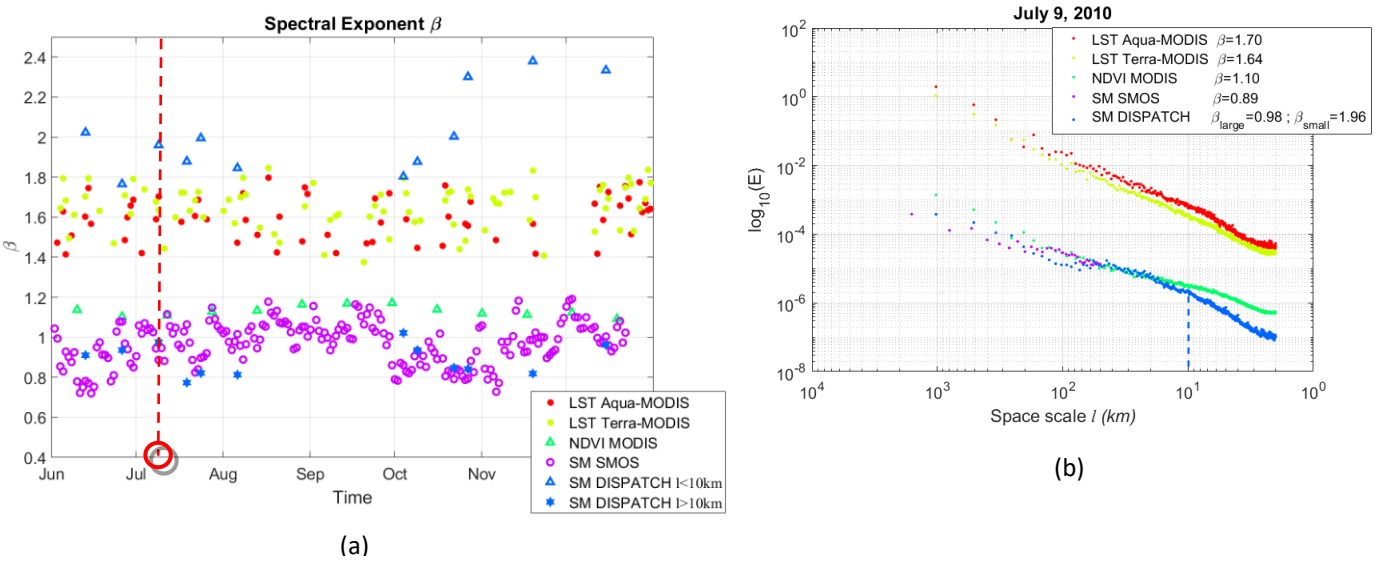

Figure 4. (a) Time series of spectral exponents over the period June-December 2010, (b) angle-integrated power spectra obtained on July 9, 2010.

5.2 Multifractal analysis

The moments of the normalized absolute gradients were estimated at all accessible resolutions. Since divergence for q greater than $q_D \approx 3$ was reported in most of the literature (Hubert et al., 2007), and because of sample size limitations, in this study moments were computed for orders set from 0 to 3, in steps of 0.1. Figure 5 shows the mean moments over the 7-month period, plotted in log-log coordinates as a function of the space scale l ($= \lambda^{-1}$). For each product, multifractal regimes are identified on specific scale ranges. The power-law described by Eq.3 is well verified over these spatial scales, corresponding to a linear variation of $log(M_l^q)$ for all orders of moments $\langle \phi_\lambda^q \rangle = M_l^q$. This behavior means that a multifractal model is well adapted on the corresponding scale ranges.

Considering vegetation and temperature MODIS products, a scaling regime is found on scales greater than 8 km (Fig.5a-c). On these scales, moments curves were fitted by linear regression (red fit lines on Fig.5), and the corresponding scaling functions $K(q)$ were computed (red, yellow and green curves Fig.5e). UM parameters were then estimated applying (derivative-free) minimization method between empirical scaling function $K(q)$ and the model form of $K(q)$ described in Eq.5. For the vegetation, parameters values are found to be α = 1.74 and C_1= 0.03 (Table.2). They are quite close to those estimated by Lovejoy et al. (2008) on similar NDVI MODIS products (α = 2 and C_1= 0.06). For Aqua surface temperature, we found the same parameter values as the vegetation ones (α = 1.7 and

C_1= 0.03), which is related to the very similar $K(q)$ functions for all orders q. Slightly different parameters are found for Terra products (α = 1.91 and C_1= 0.04). This difference could be due to the different acquisition time of the two satellites (10:30 for Terra and 13:30 for Aqua). This may have some effect on the multiscaling behavior of surface temperature. Another reason to this difference could be the larger scaling regime considered for Terra: a multifractal behavior is observed on scales ranging from 8 km to 1024 km, against 8 km to 300 km for Aqua and NDVI products. Anyway, these results confirm (NDVI) and reveal (LST, not yet studied at this time) the multifractal properties of the considered MODIS products. In both cases, they are characterized by a high degree of multifractality (α is close to 2, value corresponding to the log-normal case) and by a low dispersion of the field ($C_1 <$ 0.1).

SMOS SM products show good multifractal behavior too: moments are found to be well fitted (R^2 = 0.99, cf. Table.2), on most of the aggregation scales (apart from the 2 greatest scales, 1600 km and 800 km). Scaling function was computed over spatial scales going from the 25 km observation scale to 400 km (purple curve in *K(q)* graph, Fig.5). Compared to MODIS products, a growing divergence is noticed between SMOS and NDVI/LST scaling functions, especially for orders *q* greater than 1. This scaling behavior is confirmed by different UM parameters: α = 1.46 and C_1= 0.16. To our knowledge, no application of the UM model has already been made on remotely sensed SM from passive microwaves. Therefore, it is difficult to compare these results with literature. However, although they didn't use the UM model, Kim and Barros (2002b) studied spatial scaling properties of passive microwave SM, estimated from airborne L-band radiometer (Southern Great Plains Experiment 1997, USA). They observed a multifractal scaling on a similar scale range (1.6 km to 250 km), which is coherent with our results. Lovejoy et al. (2008) indeed applied the UM model, but on an optical SM index, estimated from MODIS reflectances (Lampkin and Yool, 2004). They found α = 2 and C_1 = 0.05 over lower spatial scales (0.5 km to 25 km). These parameter values are quite different from ours. The different scale range and the different study area (Guadalajara, central Spain, in Lovejoy et al., 2008) between their work and ours could be a possible explanation to this result. Another reason might be linked to the nature of the signal studied. Optical-estimated indexes, like MODIS SM index, are more sensitive to land cover such as vegetation (Fabre et al., 2015; Haubrock et al., 2008), then "polluting" the scaling properties of SM.

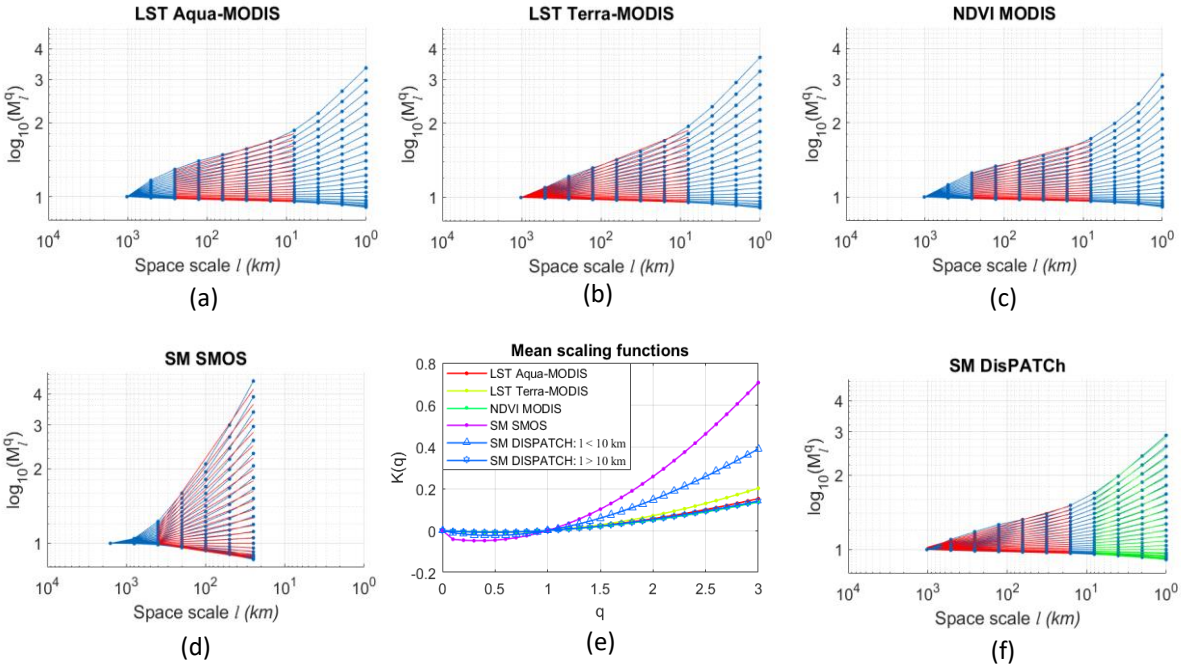

Figure 5. Mean moments as a function of space scale l in km (a-d; f) and mean scaling functions (e) of DisPATCh related products (over the full June-December period). Scaling regimes are distinguished and fitted with the straight lines (linear regressions on moments graphs).

Focusing now on disaggregated SM products, a change of slope is noticed for each of the statistical moments. The same segmentation algorithm was applied on all moment curves, revealing a scale break at about ten kilometers. Two multifractal scaling regimes may be observed here, confirming the twofold scaling behavior found in the power spectra. Considering larger scales (l > 10 km, red fit lines on Fig.5), estimated UM parameters are: α = 1.64 and C_1= 0.03. They are close to the parameters found for our MODIS products (NDVI and LST), with a high degree of multifractality and a low dispersion of the field. For smaller scales (l < 10 km, green fit lines on Fig.5), the degree of multifractality is almost unchanged (α = 1.59) compared to the large scales regime. However, the dispersion parameter is increased (C_1 = 0.09), which is three times the value obtained on greater scales. Though, the difference between the two multifractal scaling regimes seems to be mainly linked to the dispersion of SM through scales. If we refer to the multifractal analysis of MODIS SM index made by Lovejoy et al. (2008), our estimates are coherent considering α (for both ranges of scales) and C_1 (on large scales). Lovejoy et al. (2008) didn't notice any scale break, therefore it is difficult to comment our estimate of C_1 at small scales. Nevertheless, Kim and Barros (2002b) observed a similar scale break (at about the same 10 km scale) on passive microwave SM. Indeed, they noticed two scaling regimes from variance, spectra and moments graphs. The twofold scaling

behavior of DisPATCh SM products looks consistent with the scale break identified first by Kim and Barros (2002b).

PRODUCTS	Grid spacing (km)	Scale range (km)	β	$R^2{}_\beta$	α	C_1	$R^2{}_{K(q)}$	H	$R^2{}_H$
SM DISPATCH	1	[1 – 10]	2.01	0.97	1.59	0.09	0.97	0.45	0.99
		[10 – 1024]	0.89	0.92	1.64	0.03	0.96	0.15	0.98
SM SMOS	25	[25 – 1600]	0.97	0.94	1.46	0.16	0.99	0.29	0.98
LST Aqua-MODIS	≈ 1	≈ [1 – 1024]	1.60	0.98	1.7	0.03	0.96	0.26	0.98
LST Terra-MODIS	≈ 1	≈ [1 – 1024]	1.65	0.99	1.91	0.04	0.95	0.31	0.99
NDVI Terra- MODIS	≈ 1	≈ [1 – 1024]	1.13	0.98	1.74	0.03	0.96	0.15	0.99

Table 2. Scaling parameters obtained from multifractal analysis over the period June-December 2010. R^2 coefficients were estimated from linear regressions on the specified scale range. Note that $R^2{}_{K(q)}$ is the average of the coefficients obtained on every moment curves.

6 Discussion

6.1 A physically-explained twofold scaling behavior of soil moisture?

Since SM variability is impacted by several environmental factors (Brocca et al., 2007; Crown et al., 2012), the scale break observed on disaggregated SM could be the result of processes acting at different space scales. At finer scales ($l < 10\ km$), spatial structure of SM is governed by infiltration or runoff, which are mainly related to the soil properties (texture, structure) (Hawley et al., 1983; Famiglietti et al., 1998). On the other hand, at larger scales ($l > 10\ km$), SM variability is more affected by evapotranspiration processes (Mohanty and Skaggs, 2001) or precipitation (Jackson et al., 1999).

A similar scale break at ~ 10 km was also noted by Kim and Barros (2002b) based on power spectra and statistical moments of SM, estimated from airborne L-band radiometer (Southern Great Plains Experiment 1997, USA). SM retrievals were obtained at 1 km nominal resolution from the *τ-ω* model (Jackson and Schmugge, 1991) which depends on Vegetation Water Content (VWC) estimates based on NDVI. They observed that the relationship between the spatial structure of SM and landscape characteristics was strongly modulated by the wetness of the soil. Indeed, they applied an EOF analysis (Empirical Orthogonal Function) between SM and auxiliary data which are topography, VWC and soil content. This revealed that SM was much correlated to topography during rain events,

whereas stronger correlation with vegetation (water content) was noticed during drier periods (mainly governed by evapotranspiration processes).

These results are interesting since other research studies also observed similar scale break in the case of precipitation products obtained from radar at 1 km resolution (southeastern France, Gires et al., 2011). Indeed, a transition in spectra and moments was noticed at about twenty kilometers (not far from our 10 km scale break). However, some limitations relative to radar data acquisition must be taken into account considering these results. Indeed, constraints due to algorithmic processing (change from polar to Cartesian coordinates, impact of missing data, temporal integration…) and to physics (attenuation by rainfall, etc.) may impact the scaling properties of precipitation radar images. Moreover, the Z-R relationship between radar reflectivity and rain rate (Marshall and Palmer, 1948) remains somehow controversial, with a non-robust parameterization from a multi-scale point of view (Verrier et al., 2013). Thus, in this context, the scale break detected by Gires et al. (2011) may not be as relevant as it could be. However, they also analyzed the multifractal behavior of simulated precipitations generated on the same area, at ~ 2 km resolution, from the Meso-NH atmospheric model (Lafore et al., 1997). The analysis revealed the presence of a comparable scale break at about 30 km, which tends to show that this transition scale in precipitation data is not an artifact. Since rainfall is an important forcing of SM, it may be thought that a break in the rainfall spectra would affect the SM, in a more significant way when the rain event is important. Moreover, a theoretical model of SM in the time domain was proposed by Katul et al. (2007) to relate the scaling of precipitation to that of SM. The spectral exponents of these two variables were found to be connected over time scales finer than 7 days, through the simple equation: $\beta_{SM} = \beta_P + 2$ (with β_{SM} and β_P the negative spectral slopes of respectively soil moisture and precipitation time series). Despite these results were observed on time series, it may corroborate the possible dependence between the SM variability and that of heavy rainfall, even in the space domain.

Considering seasonal variations, the power spectra of disaggregated SM seem to reveal a pronounced twofold scaling behavior especially during spring and early summer (October to December period). Since DisPATCh images are mainly located over the middle-south part of the Murray Darling Basin, climate is then mostly temperate. Therefore, the last months of the study period correspond to a drier landscape. Thus, the two scaling regimes seem to be even more distinct when the soil is drier. To demonstrate this effect, the spatial mean of DisPATCh SM ($\mu(SM)$) and the absolute difference $\left|\beta_{large} - \beta_{small}\right|$ were computed for each disaggregated image. In Figure 6, the normalized anomalies of these two variables are in line with this hypothesis (blue and red circle symbols): a more pronounced twofold scaling behavior seems to be found on the driest days (Oct-Nov-Dec). Kim and Barros (2002b) noticed a similar behavior, with lower scaling differences during

rain events (observed on both spectra and moments of SM). In certain dates, they even noticed that there was no scale break at all, corresponding to very high wetness conditions of the soil. Moreover, we estimated the position of the scale breaks on each power spectrum during the period (corresponding normalized anomalies plotted in gray star symbols, Fig.6). Although it is positioned on average around 10 km (not shown here but the mean value over the full period was estimated at ~ 13 km), the transition scale between the two scaling regimes seems to follow a decreasing trend as

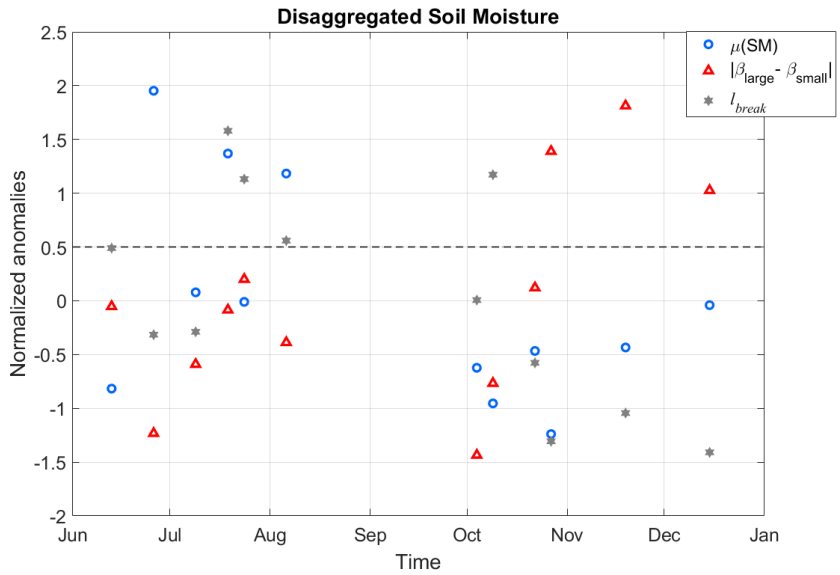

Figure 6. Time series over the period June-December 2010 of the normalized anomalies of the three following variables: the spatial mean of each DisPATCh SM product; the absolute difference between the two spectral exponents β_{large} and β_{small} (estimated respectively for $l > 10\ km$ and $l < 10\ km$); the position of the scale breaks estimated on each spectrum by the segmentation algorithm. The dotted line differentiates the two regimes: wetter trend from June to September and drier trend from October to December.

the soil is drying, with estimated scale breaks ranging from ~ 15 km in wet period to ~ 12 km in dry period. A comparable behavior was observed by Kim and Barros (2002b), showing that the position and the amplitude of the scale break in the scaling behavior of SM is dependent on the state of SM, and thus on the hydrometeorological conditions like rain, evapotranspiration and infiltration processes.

To go further on the dependences between seasons and SM scaling, Kim and Barros (2002b) observed that multifractality was almost always involved on scales smaller than 10 km, whatever the dryness of the soil. However, on scales greater that 10 km, multifractality was found to become monofractality, especially during drier conditions. At large scales (between 25 km and 400 km), a comparable effect was noticed on our SMOS SM products (purple circles, Fig.7): the multifractality

index α is decreased from around 1.6 (June) to 1.3 (December), which may reflect a moderate decrease of multifractality during the study period. Therefore, multifractal properties of SM at large scales seem to be related to the soil dryness. This may give complementary explanations to the

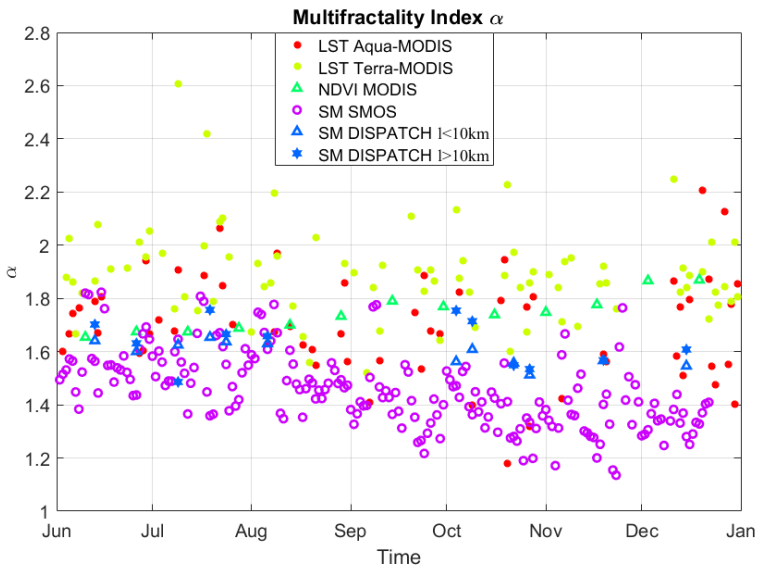

Figure 7. Time series of the multifractality index α, over the period June-December 2010.

twofold scaling behavior of SM. On the other hand, considering DisPATCh SM, a rather constant evolution of α is noticed on both small scales (blue triangle symbols) and large scales (blue star symbols). The first case confirms the idea that multifractality is not dryness-dependent on smaller scales, whereas the second is in contradiction with this assumption. Thus, the latter should be considered cautiously to explain the scaling properties of SM.

6.2 A model-induced twofold scaling behavior of soil moisture?

In relatively recent works (Mascaro et al., 2010; Mascaro and Vivoni, 2012), scale invariance and multifractality were noticed from SM products measured from airborne L-band radiometers (Southern Great Plains 1997 and 1999 Experiments, USA). In these studies, a Log-Poisson multifractal model was applied (She and Levêque, 1994), and a single scaling regime was observed on statistical moments, from 0.8 km to 25.6 km scales. Although this result confirms the multifractal properties of SM on space scales similar to ours, it refutes the existence of two scaling regimes. No scale break was observed at about ten kilometers. Since the Log-Poisson model is based on a similar universal theory as the UM model (continuous cascades), it is somewhat unexpected not to detect the same transition on comparable SM products (same technology and same scale range).

To investigate if this difference could be related to the case study (different areas or periods), we compared our DisPATCh products to fine scale airborne data acquired during the AACES-2 mission (Peischl et al., 2012). This mission was performed in September 2010, during which transect flights were carried out over the Murrumbidgee catchment. Brightness Temperatures (BT) were acquired from L-band radiometer (on both H- and V-polarizations), at a nominal 1 km spatial resolution. The study area was divided in 5 patches of 50 × 100 km², each corresponding to a single flight day (13, 16, 19, 21, 22 September). We gathered these patches into one single BT image, and we selected a sub-image of 128 × 128 km². To verify the presence of two scaling regimes in the data, we applied spectral analysis on both H-polarized and V-polarized BT sub-images. In Figure 8, the power spectrum of H-polarized BT was compared to the power spectra of DisPATCh related products on equivalent period. The spectra of each satellite product available between the 13 and 22 of September were averaged together. Since no DisPATCh SM products were pre-selected on this period (because of too many NaN), we chose the nearest available product, which corresponds to 4 October. In Figure 8, one single linear fit is observed on BT power spectrum, over the entire scale range (from 1 km to 128 km) and with a spectral slope equivalent to that of SMOS SM spectrum (β ≈ 1). Note that V-polarized spectrum was not plotted here, but it was found to be very similar to the H-polarized one.

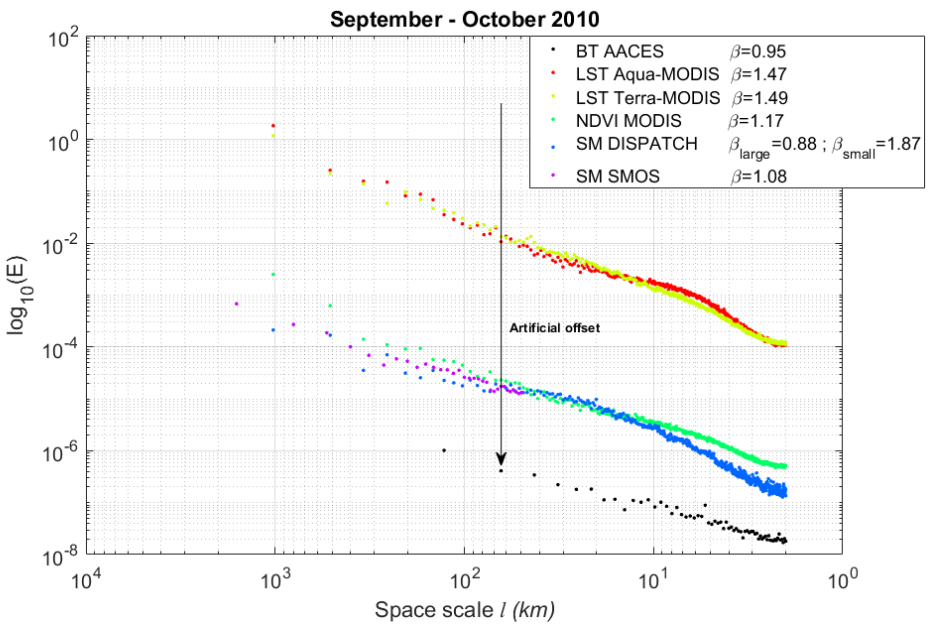

Figure 8. Angle-integrated power spectra of Brightness Temperature (BT) and DisPATCh related products, obtained on the period September-October 2010. For better visualization and comparison, BT power spectrum was shifted down (black arrow on the graph).

Different scaling behaviors were noticed for AACES BT and DisPATCh SM, on similar area and similar period. This may sustain the idea that the scale break observed at 10 km could be caused by the DisPATCh model and, specifically, by the way in which the multi-scale properties of each product

are mixed in the algorithm. To verify this hypothesis, *a simplified version of the C4DIS processor* was implemented in order to study the multi-scale behavior of the different variables combined and generated through the algorithm. To do this, the method proposed by Molero et al. (2016) was followed, which includes the two main steps described in section 4.2: (1) the estimation of SEE_{HR} variable (Soil Evaporative Efficiency) from MODIS products (Eq.13-15) and (2) the proper disaggregation process of SM from SMOS products, SEE_{HR} and SM_p parameter (Eq.17-18).

According to this method, our algorithm was applied on SMOS and MODIS products acquired on November 19, 2010. A sub-area was selected (≈ 700 x 700 km²) in order to have a smaller number of missing data, and thus to get the minimum impact of gap-filling on the studied products. Figure 9 shows the power spectra obtained from the input products of DisPATCh (LST, NDVI), intermediate products (T_s, SEE) and output product (SM MEAN). The latter product is the average of the 6 disaggregated SM images obtained from the 6 SM-LST combinations (see section 4.1). Here, just one SMOS image of ≈25 km grid spacing was combined with the MODIS products. Indeed, both cases with one SMOS image and four downsampled ones were implemented (section 4.1 and Molero et al., 2016), and no significant differences were observed between the final products and between their power spectra. Therefore, for simplicity of implementation, only the case of one SMOS image was considered here. For comparison, the power spectrum of C4DIS SM product acquired on the same date and on the same sub-area was also plotted here. The segmentation algorithm used in section 5 was applied on each power spectrum. A geometric mean was estimated from the different scale breaks obtained, revealing two averaged scale breaks which are nearly common to all spectra: the first at almost ten kilometers (l = 9 km) and the second at about thirty kilometers ($l = 33$ km). To evaluate the link between the multi-scale behavior of each product, spectral exponents were estimated on the two following scale ranges: from 33 km to 9 km (*large scales*) and from 9 km to 1 km (*small scales*). Comparing our SM MEAN product with SM C4DIS product (Table.3), a very similar scaling is observed on *large scales* (β_{large} ≈ 1.3). On *small scales*, high spectral exponents are found, with β_{small} ≈ 2 for SM MEAN and β_{small} = 2.86 for SM C4DIS. These different spectral slopes on finer scales could be related to the non-implementation of some filtering steps in our algorithm which are indeed coded in C4DIS processor: corrections of topography effects, filtering LST data with low quality, etc. (Molero et al., 2016).

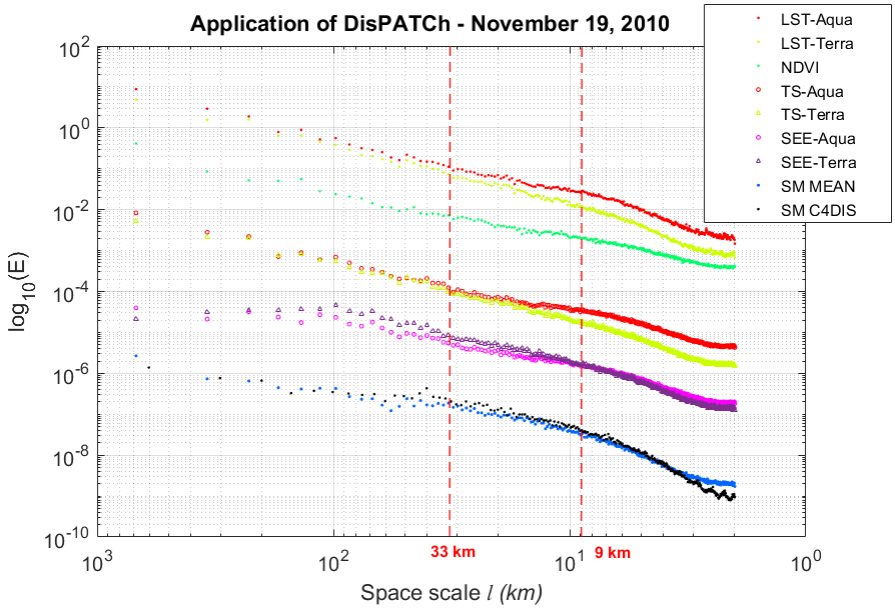

Figure 9. Angle-integrated power spectra of some of the input, intermediate and output products obtained from our implementation of DisPATCh on November 19, 2010. Power spectrum of the final C4DIS product is also plotted here. For better visualization and comparison, the positions of power spectra according to Y axis were modified.

Despite these small differences between SM MEAN and SM C4DIS spectra, the scale break remains noticeable, as it seems to be on the other products of the algorithm. To demonstrate this, the absolute difference $\Delta\beta = |\beta_{large} - \beta_{small}|$ was computed as an indicator of the amplitude of the scale break. Values greater than 0.6 were found for LST (Aqua and Terra), T_s (Aqua) and SEE (Aqua) products. These results seem to reveal that MODIS LST products would be the cause of the scale break located at about ten kilometers in the disaggregated SM product. This scale break would propagate in the algorithm through the estimation of T_s and SEE. A possible explanation to this scale break in LST products may be related to the physical nature of the signal used. Indeed, optical/thermal sensors can be characterized by modified spectral slopes near the satellite resolution. Moreover, this effect seems more important on Aqua LST ($\Delta\beta$ = 0.83) than on Terra LST ($\Delta\beta$ = 0.62). Similar differences can be observed between the mean power spectra of Aqua and Terra LST over the full period (Fig.3 in section 5.1). Thus, it may be thought that the amplitude of the scale break could be related to the diurnal cycle of surface temperature. Since surface temperatures measured from Aqua are acquired at the hottest hours of the day (13:30), there might be a correlation between the amplitude of scale break and the level of surface temperature.

Scale range (km)	[33 - 9]		[9 - 1]		Δβ
Spectral exponent	β	$R^2{}_\beta$	β	$R^2{}_\beta$	
LST - ***Aqua***	1.08	0.97	1.91	0.98	0.83
LST - ***Terra***	1.39	0.97	2.01	0.98	0.62
NDVI	0.93	0.94	1.22	0.98	0.29
TS - ***Aqua***	0.90	0.95	1.55	0.98	0.65
TS - ***Terra***	1.33	0.98	1.79	0.98	0.46
SEE - ***Aqua***	0.88	0.96	1.61	0.98	0.73
SEE - ***Terra***	1.25	0.97	1.83	0.98	0.58
SM MEAN	1.22	0.96	2.08	0.97	0.86
SM C4DIS	1.29	0.96	2.86	0.98	1.57

Table 3. Spectral exponents obtained from spectral analysis of DisPATCh related products on November 19, 2010 (Fig.9). R^2 coefficients were estimated from linear regressions on the specified scale range. $\Delta\beta = |\beta_{large} - \beta_{small}|$ is used as an indicator of the amplitude of the scale break, with *large* and *small* referring respectively to [33 – 9] km and [9 – 1] km scale ranges.

Considering the scale break observed at about 30 km, this one may not be related to the multi-scale properties of MODIS products but possibly to the combination of different products defined on different grid spacings. Indeed, DisPATCh algorithm combines and creates products which have either the grid spacing of MODIS data (≈1 km) or the grid spacing of SMOS data (≈25 km). For example, the estimation of SEE (Eq.15) combines end-members ($T_{s,max}$ and $T_{s,min}$) defined on the SMOS grid, with another product (T_s) defined on the MODIS grid. As seen on Figure 10, a footprint of SMOS pixels is then observable on the resulting image of SEE. This property is due to the resampling strategy of SMOS data and to the end-members that are defined on the SMOS grid. This systematic footprint is visible in the real domain but can also have an impact in the Fourier domain. Indeed, sharp transitions at the SMOS pixels limits may create spurious convolutions by cardinal sine-like functions which may affect the spectrum. On the disaggregated SM, this effect can generate an imperfect transition between the part of the spectrum related to SMOS SM (l > 25 km) and the part related to MODIS products (l < 25 km). Regarding the behavior of SEE power spectra on scales greater than thirty kilometers (Fig.9), a lower spectral slope is observed (β ≈ 0.5) comparing to that obtained on finer scales (β ≈ 1 for $[33 - 9]\ km$). This could be related to the oversampling of SMOS

data, generating harmonics on fine scales and therefore not including variability on large scales. In this manner, not only large scales but even fine scales could be affected by this effect. The latter may also contribute, in a way, to the accentuation of the spectral drop observed at finer scales on the final disaggregated SM product.

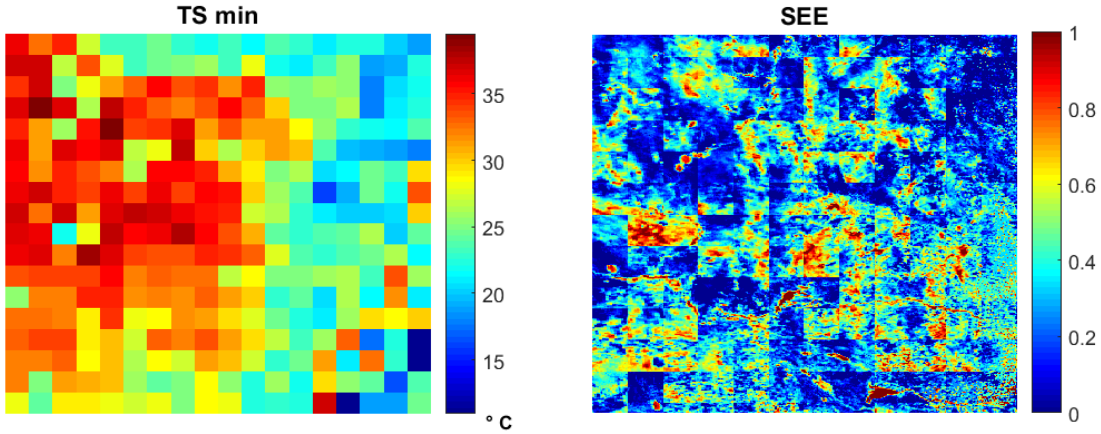

Figure 10. Images corresponding to $T_{s,min}$ and SEE_{HR} products obtained from our implementation of DisPATCh on November 19, 2010.

7 Conclusion

During the last century, several studies were carried out to investigate the scaling properties of SM. Very diversified technologies were used to access and study the spatial structure of SM: airborne microwaves products, satellite optical indices, etc. Moreover, different approaches have been considered, such as power spectra, statistical moments, fractal dimensions, and even different types of cascade models (Log-Poisson, Universal Multifractal, and even no explicit parameterization in some cases…). In this study, we analyzed the multifractal behavior of remotely sensed SM products over space scales ranging from the kilometric field scale to the continental scale. Universal Multifractal model was applied for the first time on SMOS SM data, giving access to large scale variabilities of SM, over the Australian landscape. Fractal and multifractal properties were observed, which confirmed and completed some results reported in existing literature.

The relevant aspect of the present work may be the multi-scale analysis of the outputs of the disaggregation algorithm DisPATCh (Merlin et al., 2008a; Molero et al., 2016). This deterministic algorithm improves the space resolution of SMOS SM products from 40 km to 1 km. To do this, it

combines coarse-scale SMOS SM with fine-scale (≈1 km) MODIS optical/thermal data. Although several validation studies have been realized on this downscaling method (Malbéteau et al., 2016; Merlin et al., 2012, 2013, 2015; Molero et al., 2016), none fully explored its statistical behavior over a continuum of space scales. In this context, we applied fractal and multifractal analysis on the different products involved in DisPATCh algorithm, including disaggregated (and original) SM products, and MODIS auxiliary data which are vegetation indices (NDVI) and surface temperatures (LST).

Input products of DisPATCh revealed relatively good scaling properties over the considered scale ranges. Indeed, NDVI, LST and original SM were characterized by a power law evolution of their power spectra and statistical moments, meaning respectively fractality and multifractality. However, a specific scaling behavior was noticed for the output disaggregated SM. Two scaling regimes were obtained, with a transition scale observed at about ten kilometers, on both spectra and moments. Considering spectral analysis, on large scales (l > 10 km), disaggregated SM was found to have the same scaling as the original SM measured from satellite. On finer scales (l < 10 km), a different behavior was noticed, with an increasing slope of the power spectrum. Similar scale break was detected on statistical moments, showing that both spectral and multifractal properties of DisPATCh SM are characterized by this twofold scaling signature.

Two possible arguments were given to explain the specific scaling of the disaggregated SM. First, a more physical interpretation may indicate that this twofold scaling behavior would be related to the real properties of SM. As it was previously observed by Kim and Barros (2002b), such scale break would be reflective of nonlinear hydrometeorological processes (rainfall, infiltration, evapotranspiration) acting at different space scales and modulated by terrain, soils and vegetation distributions. The spatial structure of SM may be more impacted by infiltration or runoff at the field scale, whereas it would be mainly controlled by evapotranspiration or precipitation at the regional/continental scale. A more significant scaling transition was observed on the driest days (early summer), which may support the link between SM and external forcing agents such as precipitation.

A second explanation would be more algorithmic and directly related to the processing of the different products used and created within the algorithm. The model used in DisPATCh would generate SM whose statistics are not properly distributed across scales. This may occur at two levels in the algorithm. First, some MODIS products properties (such as breaks in the scaling) may be retrieved in the final DisPATCh products. Indeed, a spectral drop at about the same ten kilometers scale was detected on LST power spectra. Although it is less pronounced than on disaggregated SM,

this scale break may be introduced by MODIS LST and amplified by the disaggregation model. Since one single scaling regime was noticed on Brightness Temperature (BT) products acquired in the L-band over the same area and the same period, these observations suggest that the unexpected scaling in MODIS products would be caused by the technology specific to optical/thermal sensors. Then, another impact of the algorithm on the multi-scale properties of SM may be related to signal processing artifacts occurring with the combination of several products defined with different grid spacings. This combination is required to permit conservativity between input and output SM products. However, from a signal processing point of view, this could create systematic footprints on the final image (i.e., visible SMOS pixels in the downscaled products) and therefore affect the power spectrum (convolutions by cardinal sine-like functions).

At this point, it is difficult to determine which of the physical or algorithmic factors would be at the origin of this twofold scaling behavior. Though, a plausible hypothesis may be that both factors could affect the scaling of disaggregated SM. Indeed, a scale break at about the SMOS SM resolution could be initially produced by combination artifacts, which would be more or less amplified in the algorithm according to seasonal conditions, resulting in moving the scale break during the period to finer scales.

Further work need to be addressed to fully explain these results, in particular to determine to what extent each of the two factors impacts the scaling of DisPATCh SM. Complementary auxiliary data should be compared to our products. Indeed, an EOF or comparable analysis made on DisPATCh SM and topography, vegetation water content or soil content would provide relevant information about the connection between the spatial variability of these products and help with interpretation. Moreover, it would be interesting to verify if precipitation products can be characterized by a similar scale break on equivalent space scales and over the same area (Murray Darling Basin). However, it must be considered that such a comparison might be complex to interpret since, to our knowledge, no theoretical model has been proposed yet to relate the spatial scaling properties of SM and that of rainfall (as it was already done in the time domain by Katul et al., 2007). In the same way, the comparison between DisPATCh SM and airborne BT is not that trivial, because relatively complex operations are involved to get inverted SM from BT. To illustrate this, Mascaro and Vivoni (2012) noticed monofractality from BT data, whereas multifractality was observed from the corresponding inverted SM data. The scaling properties of BT could be affected during the inversion process, explaining why the single scaling we observed on BT does not imply single scaling of DisPATCh SM. Therefore, multifractal analysis of proper fine scale SM products may clarify this idea and help validating DisPATCh SM variability.

In the hypothesis of a model-induced scale break, current work is engaged to quantify the effect of MODIS products and the trace of pixel SMOS on different dates and on proper operational conditions (analysis of products used and generated within the C4DIS processor). An application of DisPATCh using Landat-7 auxiliary data instead of MODIS products was realized by Merlin et al. (2013), allowing a disaggregation process at sub-kilometric scales (100 m). Since Landsat-7 provides optical/thermal data with higher resolution than MODIS, it could be interesting to verify if both Landsat-7 and the resulting disaggregated SM product would be characterized by a similar scale break, but shifted on finer scales than the 10 km scale observed on MODIS. Therefore, the results obtained could help to quantify the real impact of optical/thermal auxiliary data on the multi-scale properties of DisPATCh SM. On a more operational point a view, if this impact is confirmed, the results obtained may help to define a specific scale below which the variability generated by the disaggregation model may not be as reliable as it should be. Concerning the impact of SMOS pixels footprint effects on the disaggregated product, a solution could be to filter out the sharp transitions at SMOS pixels limits. However, this should be done with caution since such filters may excessively attenuate the variance at smaller scales. Another way to investigate our observations of DisPATCh SM is to focus on its dynamical behavior over different aggregation scales. Indeed, one of the main problem in downscaling a dynamical behavior arises from the fact that the dynamical behavior of an aggregated signal can be approximated by the same deterministic equation structure only when the aggregated area is phase-synchronized (Mangiarotti et al., 2016). Considering this issue, the applicability of deterministic downscaling methods like DisPATCh may not be that obvious over certain spatial scales, leading to several difficulties and, perhaps, contributing to explain the scaling irregularities observed in this study.

Finally, a possibility could be to compare the SM variability produced by DisPATCh with that created by fractal stochastic downscaling methods. Based on scaling properties, these methods preserve the probability distribution from large to fine scales. In precipitation, several studies applied these algorithms on rainfall data (Rebora et al., 2006; Sharma et al., 2007). Research works proposed methods developed on multiplicative cascade such as Log-Poisson (Deidda, 2000) or UM model (Gires et al., 2012), revealing some potential to quantify uncertainty and representativeness errors between coarse-scale and in-situ measurements. Concerning SM downscaling, some studies used such fractal-based methods (Bindlish and Barros, 2002; Kim and Barros, 2002a; Mascaro et al., 2010). In our study, it may be interesting to apply this kind of method on SMOS products. This would consists in injecting in the UM model the values of α and C_1 parameters obtained from SMOS products on large scales, and then continuing the cascade at higher resolutions. Following this procedure, the fine-scale field will have the same scaling properties as the coarse-scale one.

However, since the disaggregation is based on random generator, an ensemble of possible fields can be proposed from just one pair of α/C_1 parameter. Therefore, this kind of methodology may not be fully suitable in the case of operational hydro-agricultural applications, in particular when determining the position of the extremes. To overcome this inconvenient, a combination of the two approaches may be an interesting compromise between statistical scaling and evaporation-based determinism. For example, in DisPATCh algorithm, an idea might be to find a modified estimator of SEE that would be used in the disaggregation equation (18). This modified SEE would be computed by applying a 2D filter on the original SEE, which would be actually equivalent to perform a fractional integration of order $\Delta H = H_{requested} - H_{non\text{-}filtered}$ with $H_{requested}$ and $H_{non\text{-}filtered}$ measured respectively from SMOS soil moisture (at large scales) and from non-filtered SEE (for scales under 10 km). Doing this, the spectral slope of SEE may be adjusted, like that of the final disaggregated soil moisture. Thus, coarse-scale and fine-scale fields could be related through a common degree of fractional integration, which may contribute to limit the twofold scaling behavior observed on the disaggregated product. In practice, this modification would not be easy to implement since the filtering should be properly dimensioned in order to affect only the small scales, between 1 and 10 km. Moreover, this texture-based image correction may impact the physical properties of SEE, so there would be a compromise to be made on this aspect.

Acknowledgements

We are grateful to C. Rüdiger and J. Walker from Monash University (Melbourne, Australia) for their advice and for giving us access to AACES data (http://www.moisturemap.monash.edu.au/aaces/). We also want to thank the SMOS team, particularly A. Mialon and A. Al Bitar for fruitful discussions.

This study was supported by the “Région Occitanie” (France) and “IUT Paul Sabatier” (Toulouse, France). SMOS products were acquired from the “Centre Aval de Traitement des Données SMOS” (CATDS), which is the French ground segment developed by the “Centre National d’Etudes Spatiales” (CNES, France) in collaboration with IFREMER (Brest, France). MODIS products were obtained from the Land Processes Distributed Active Archive Center (LP DAAC), operating as a partnership between the NASA and the U.S. Geological Survey (USGS).

References

Akbar, R., & Moghaddam, M. (2015). A Combined Active–Passive Soil Moisture Estimation Algorithm With Adaptive Regularization in Support of SMAP. *IEEE Transactions on Geoscience and Remote Sensing*, *53*(6), 3312-3324. https://doi.org/10.1109/TGRS.2014.2373972

Al Bitar, A., Leroux, D., Kerr, Y. H., Merlin, O., Richaume, P., Sahoo, A., & Wood, E. F. (2012). Evaluation of SMOS Soil Moisture Products Over Continental U.S. Using the SCAN/SNOTEL Network. *IEEE Transactions on Geoscience and Remote Sensing*, *50*(5), 1572-1586. https://doi.org/10.1109/TGRS.2012.2186581

Albergel, C., Brocca, L., Wagner, W., de Rosnay, P., & Calvet, J. C. (2013). Selection of performance metrics for global soil moisture products: The case of ascat soil moisture product. *Remote sensing of energy fluxes and soil moisture content* (pp. 431–448).

Anderson, M. C., Norman, J. M., Mecikalski, J. R., Otkin, J. A., & Kustas, W. P. (2007). A climatological study of evapotranspiration and moisture stress across the continental United States based on thermal remote sensing: 2. Surface moisture climatology. *Journal of Geophysical Research*, *112*(D11). https://doi.org/10.1029/2006JD007507

Bárdossy, A., & Lehmann, W. (1998). Spatial distribution of soil moisture in a small catchment. Part 1: geostatistical analysis. *Journal of Hydrology*, *206*(1-2), 1-15. https://doi.org/10.1016/S0022-1694(97)00152-2

Bartalis, Z., Wagner, W., Naeimi, V., Hasenauer, S., Scipal, K., Bonekamp, H., & Anderson, C. (2007). Initial soil moisture retrievals from the METOP-A Advanced Scatterometer (ASCAT). *Geophysical Research Letters*, *34*(20). https://doi.org/10.1029/2007GL031088

Bindlish, R., & Barros, A. P. (2002). Subpixel variability of remotely sensed soil moisture: An inter-comparison study of SAR and ESTAR. *IEEE Transactions on Geoscience and Remote Sensing*, *40*(2), 326-337. https://doi.org/10.1109/36.992792

Brocca, L., Morbidelli, R., Melone, F., & Moramarco, T. (2007). Soil moisture spatial variability in experimental areas of central Italy. *Journal of Hydrology*, *333*(2-4), 356-373. https://doi.org/10.1016/j.jhydrol.2006.09.004

Brocca, L., Tullo, T., Melone, F., Moramarco, T., & Morbidelli, R. (2012). Catchment scale soil moisture spatial–temporal variability. *Journal of Hydrology*, *422-423*, 63-75. https://doi.org/10.1016/j.jhydrol.2011.12.039

Budyko, M. I. (1961). The heat balance of the earth's surface. *Soviet Geography*, *2*(4), 3-13. https://doi.org/10.1080/00385417.1961.10770761

Busch, F. A., Niemann, J. D., & Coleman, M. (2012). Evaluation of an empirical orthogonal function-based method to downscale soil moisture patterns based on topographical attributes: DOWNSCALING SOIL MOISTURE PATTERNS BASED ON TOPOGRAPHICAL ATTRIBUTES. *Hydrological Processes*, *26*(18), 2696-2709. https://doi.org/10.1002/hyp.8363

Carlson, T. (2007). An Overview of the « Triangle Method » for Estimating Surface Evapotranspiration and Soil Moisture from Satellite Imagery. *Sensors*, *7*(8), 1612-1629. https://doi.org/10.3390/s7081612

Carlson, T. N., Gillies, R. R., & Perry, E. M. (1994). A method to make use of thermal infrared temperature and NDVI measurements to infer surface soil water content and fractional vegetation cover. *Remote Sensing Reviews*, *9*(1-2), 161-173. https://doi.org/10.1080/02757259409532220

Cayan, D. R., & Georgakakos, K. P. (1995). Hydroclimatology of Continental Watersheds : 2. Spatial Analyses. *Water Resources Research*, *31*(3), 677-697. https://doi.org/10.1029/94WR02376

Chauhan, N. S., Miller, S., & Ardanuy, P. (2003). Spaceborne soil moisture estimation at high resolution: a microwave-optical/IR synergistic approach. *International Journal of Remote Sensing*, *24*(22), 4599-4622. https://doi.org/10.1080/0143116031000156837

Choi, M., & Hur, Y. (2012). A microwave-optical/infrared disaggregation for improving spatial representation of soil moisture using AMSR-E and MODIS products. *Remote Sensing of Environment*, *124*, 259-269. https://doi.org/10.1016/j.rse.2012.05.009

Collow, T. W., Robock, A., Basara, J. B., & Illston, B. G. (2012). Evaluation of SMOS retrievals of soil moisture over the central United States with currently available in situ observations: EVALUATION OF SMOS WITH IN SITU DATA. *Journal of Geophysical Research: Atmospheres*, *117*(D9), n/a-n/a. https://doi.org/10.1029/2011JD017095

Crow, W. T., Berg, A. A., Cosh, M. H., Loew, A., Mohanty, B. P., Panciera, R., de Rosnay, P., Ryu, D., & Walker, J. P. (2012). Upscaling sparse ground-based soil moisture observations for the validation of coarse-resolution satellite soil moisture products: UPSCALING SOIL MOISTURE. *Reviews of Geophysics*, *50*(2). https://doi.org/10.1029/2011RG000372

D'Errico, Shape Language Modelling, https ://fr.mathworks.com/matlabcentral/_leexchange/24443-slm-shape-language-modeling, (16 April 2017).

Dai, A., Trenberth, K. E., & Qian, T. (2004). A Global Dataset of Palmer Drought Severity Index for 1870–2002: Relationship with Soil Moisture and Effects of Surface Warming. *Journal of Hydrometeorology*, *5*(6), 1117-1130. https://doi.org/10.1175/JHM-386.1

Das, N. N., Entekhabi, D., & Njoku, E. G. (2011). An algorithm for merging SMAP radiometer and radar data for high-resolution soil-moisture retrieval. *IEEE Transactions on Geoscience and Remote Sensing*, *49*(5), 1504-1512.

Das, N. N., & Mohanty, B. P. (2006). Root zone soil moisture assessment using remote sensing and vadose zone modeling. *Vadose Zone Journal*, *5*(1), 296-307.

de Montera, L., Barthès, L., Mallet, C., & Golé, P. (2009). Rain universal multifractal parameters revisited with dual-beam spectropluviometer measurements. *J Hydrometeorol*, *10*, 493.

Deidda, R. (2000). Rainfall downscaling in a space-time multifractal framework. *Water Resources Research*, *36*(7), 1779-1794. https://doi.org/10.1029/2000WR900038

Djamai, N., Magagi, R., Goïta, K., Merlin, O., Kerr, Y., & Roy, A. (2016). A combination of DISPATCH downscaling algorithm with CLASS land surface scheme for soil moisture estimation at fine scale during cloudy days. *Remote Sensing of Environment*, *184*, 1-14. https://doi.org/10.1016/j.rse.2016.06.010

Dobriyal, P., Qureshi, A., Badola, R., & Hussain, S. A. (2012). A review of the methods available for estimating soil moisture and its implications for water resource management. *Journal of Hydrology*, *458-459*, 110-117. https://doi.org/10.1016/j.jhydrol.2012.06.021

Dubrulle, B. (1994). Intermittency in fully developed turbulence: Log-Poisson statistics and generalized scale covariance. *Physical review letters*, *73*(7), 959. Consulté à l'adresse https://journals.aps.org/prl/abstract/10.1103/PhysRevLett.73.959

Engman, E. T. (1991). Applications of microwave remote sensing of soil moisture for water resources and agriculture. *Remote Sensing of Environment*, *35*(2-3), 213-226. https://doi.org/10.1016/0034-4257(91)90013-V

Entekhabi, D., Njoku, E. G., O'Neill, P. E., et al. (2010a). The soil moisture active passive (SMAP) mission. *Proceedings of the IEEE*, *98*(5), 704-716. https://doi.org/10.1109/JPROC.2010.2043918

Entekhabi, D., Reichle, R. H., Koster, R. D., & Crow, W. T. (2010b). Performance Metrics for Soil Moisture Retrievals and Application Requirements. *Journal of Hydrometeorology*, *11*(3), 832-840. https://doi.org/10.1175/2010JHM1223.1

Entin, J. K., Robock, A., Vinnikov, K. Y., Hollinger, S. E., Liu, S., & Namkhai, A. (2000). Temporal and spatial scales of observed soil moisture variations in the extratropics. *Journal of Geophysical Research: Atmospheres*, *105*(D9), 11865-11877. https://doi.org/10.1029/2000JD900051

Fabre, S., Briottet, X., & Lesaignoux, A. (2015). Estimation of Soil Moisture Content from the Spectral Reflectance of Bare Soils in the 0.4–2.5 µm Domain. *Sensors*, *15*(2), 3262-3281. https://doi.org/10.3390/s150203262

Famiglietti, J.S., Rudnicki, J. W., & Rodell, M. (1998). Variability in surface moisture content along a hillslope transect: Rattlesnake Hill, Texas. *Journal of Hydrology*, *210*(1-4), 259-281. https://doi.org/10.1016/S0022-1694(98)00187-5

Famiglietti, J.S., Ryu, D., Berg, A. A., Rodell, M., & Jackson, T. J. (2008). Field observations of soil moisture variability across scales: SOIL MOISTURE VARIABILITY ACROSS SCALES. *Water Resources Research*, *44*(1). https://doi.org/10.1029/2006WR005804

Gagnon, J.-S., Lovejoy, S., & Schertzer, D. (2006). Multifractal earth topography. *Nonlinear Processes in Geophysics*, *13*(5), 541–570.

Gires, A., Onof, C., Maksimovic, C., Schertzer, D., Tchiguirinskaia, I., & Simoes, N. (2012). Quantifying the impact of small scale unmeasured rainfall variability on urban runoff through multifractal downscaling : A case study. *Journal of Hydrology*, *442-443*, 117-128. https://doi.org/10.1016/j.jhydrol.2012.04.005

Gires, A., Tchiguirinskaia, I., Schertzer, D., & Lovejoy, S. (2011). Analyses multifractales et spatio-temporelles des précipitations du modèle Méso-NH et des données radar. *Hydrological Sciences Journal*, *56*(3), 380-396. https://doi.org/10.1080/02626667.2011.564174

Gupta, V.K., & Waymire, E.C. (1997). Reply. *Journal of Applied Meteorology*. 36, 1304.

Haubrock, S. -N., Chabrillat, S., Lemmnitz, C., & Kaufmann, H. (2008). Surface soil moisture quantification models from reflectance data under field conditions. *International Journal of Remote Sensing*, *29*(1), 3-29. https://doi.org/10.1080/01431160701294695

Hawley, M. E., Jackson, T. J., & McCuen, R. H. (1983). Surface soil moisture variation on small agricultural watersheds. *Journal of Hydrology*, *62*(1-4), 179-200. https://doi.org/10.1016/0022-1694(83)90102-6

Hu, Z., Islam, S., & Cheng, Y. (1997). Statistical characterization of remotely sensed soil moisture images. *Remote Sensing of Environment*, *61*(2), 310-318. https://doi.org/10.1016/S0034-4257(97)89498-9

Hubert, P., Tchiguirinskaia, I., Schertzer, D., Bendjoudi, H., & Lovejoy, S. (2007). Predetermination of floods. In *Extreme Hydrological Events: New Concepts for Security*, NATO Sci. Ser., IV, edited by O. F. Vasiliev et al., pp. 185–198, vol. 78, Springer, Berlin.

Hubert, P., Tessier, Y., Lovejoy, S., Schertzer, D., Schmitt, F., Ladoy, P., Carbonnel, J. P., Violette, S., & Desurosne, I. (1993). Multifractals and Extreme Rainfall Events. *Geophysical Research Letters*, *20*(10), 931-934. https://doi.org/10.1029/93GL01245

Ines, A. V. M., Mohanty, B. P., & Shin, Y. (2013). An unmixing algorithm for remotely sensed soil moisture: AN UNMIXING ALGORITHM FOR REMOTELY SENSED SOIL MOISTURE. *Water Resources Research*, *49*(1), 408-425. https://doi.org/10.1029/2012WR012379

Jackson, T. J., Le Vine, D. M., Hsu, A. Y., Oldak, A., Starks, P. J., Swift, C. T., Isham J. D., Haken, M. (1999). Soil moisture mapping at regional scales using microwave radiometry: the Southern Great Plains Hydrology Experiment. *IEEE Transactions on Geoscience and Remote Sensing*, *37*(5), 2136-2151. https://doi.org/10.1109/36.789610

Jackson, T. J., & Schmugge, T. J. (1991). Vegetation effects on the microwave emission of soils. *Remote Sensing of Environment*, *36*(3), 203-212. https://doi.org/10.1016/0034-4257(91)90057-D

Jana, R. B. (2010), *Scaling characteristics of soil hydraulic parameters at varying spatial resolutions*, PhD dissertation thesis, Tex. A&M Univ., College Station

Kaheil, Y. H., Gill, M. K., McKee, M., Bastidas, L. A., & Rosero, E. (2008). Downscaling and Assimilation of Surface Soil Moisture Using Ground Truth Measurements. *IEEE Transactions on Geoscience and Remote Sensing*, *46*(5), 1375-1384. https://doi.org/10.1109/TGRS.2008.916086

Katul, G. G., Porporato, A., Daly, E., Oishi, A. C., Kim, H.-S., Stoy, P. C., Juang, J.-Y., & Siqueira, M. B. (2007). On the spectrum of soil moisture from hourly to interannual scales: SPECTRUM OF SOIL MOISTURE CONTENT. *Water Resources Research*, *43*(5). https://doi.org/10.1029/2006WR005356

Kerr, Y., Jacquette, E., Al Bitar, A., Cabot, F., Mialon, A., Richaume, P., & Wigneron, J. P. (2013). CATDS SMOS L3 soil moisture retrieval processor: Algorithm theoretical baseline document (ATBD). *CESBIO: Toulouse, France*.

Kerr, Y. H., Waldteufel, P., Richaume, P., Wigneron, J. P., Ferrazzoli, P., Mahmoodi, A., Al Bitar, A., Cabot, F., Gruhier, C., Juglea, S. E., Leroux, D., Mialon, A., & Delwart, S. (2012). The SMOS Soil Moisture Retrieval Algorithm. *IEEE Transactions on Geoscience and Remote Sensing*, *50*(5), 1384-1403. https://doi.org/10.1109/TGRS.2012.2184548

Kerr, Y. H., Waldteufel, P., Wigneron, J.-P., Delwart, S., Cabot, F., Boutin, J., Escorihuela, M.-J., Font, J., Reul, N., Gruhier, C., Juglea, S. E., Drinkwater, M. R., Hahne, A., Martín-Neira, M., & Mecklenburg, S. (2010). The SMOS Mission: New Tool for Monitoring Key Elements ofthe Global Water Cycle. *Proceedings of the IEEE*, *98*(5), 666-687. https://doi.org/10.1109/JPROC.2010.2043032

Kim, G., & Barros, A. P. (2002a). Downscaling of remotely sensed soil moisture with a modified fractal interpolation method using contraction mapping and ancillary data. *Remote Sensing of Environment*, *83*(3), 400–413. Consulté à l'adresse http://www.sciencedirect.com/science/article/pii/S0034425702000445

Kim, G., & Barros, A. P. (2002b). Space–time characterization of soil moisture from passive microwave remotely sensed imagery and ancillary data. *Remote Sensing of Environment*, *81*(2-3), 393-403. https://doi.org/10.1016/S0034-4257(02)00014-7

Kim, J., & Hogue, T. S. (2012). Improving Spatial Soil Moisture Representation Through Integration of AMSR-E and MODIS Products. *IEEE Transactions on Geoscience and Remote Sensing*, *50*(2), 446-460. https://doi.org/10.1109/TGRS.2011.2161318

Kolmogorov, A. N. (1940). The Wiener spiral and some other interesting curves in Hilbert space. In *Dokl. Akad. Nauk SSSR* (Vol. 26, No. 2, pp. 115-118).

Kolmogorov, A. N. (1941). The local structure of turbulence in incompressible viscous fluid for very large Reynolds numbers. In *Dokl. Akad. Nauk SSSR* (Vol. 30, p. 299–303).

Kolmogorov, A. N. (1962). A refinement of previous hypotheses concerning the local structure of turbulence in a viscous incompressible fluid at high Reynolds number. *Journal of Fluid Mechanics*, *13*(01), 82. https://doi.org/10.1017/S0022112062000518

Korres, W., Reichenau, T. G., Fiener, P., Koyama, C. N., Bogena, H. R., Cornelissen, T., Baatz, R., Herbst, M., Diekkrüger, B., Vereecken, H., & Schneider, K. (2015). Spatio-temporal soil moisture patterns – A meta-analysis using plot to catchment scale data. *Journal of Hydrology*, *520*, 326-341. https://doi.org/10.1016/j.jhydrol.2014.11.042

Laferrière, A., & Gaonac'h, H. (1999). Multifractal properties of visible reflectance fields from basaltic volcanoes. *Journal of Geophysical Research: Solid Earth*, *104*(B3), 5115-5126. https://doi.org/10.1029/1998JB900023

Lafore, J. P., Stein, J., Asencio, N., Bougeault, P., Ducrocq, V., Duron, J., Fischer, C., Masson, V., Pinty, J. P., Redelsperger, J. L., & Richard, E. (1997). The Meso-NH Atmospheric Simulation System. Part I: adiabatic formulation and control simulations. *Annales Geophysicae*, *16*(1), 90-109. https://doi.org/10.1007/s00585-997-0090-6

Lampkin, D. J., & Yool, S. R. (2004). Monitoring mountain snowpack evolution using near-surface optical and thermal properties. *Hydrological Processes*, *18*(18), 3527-3542. https://doi.org/10.1002/hyp.5797

Lavallée, D., Lovejoy, S., Schertzer, D., & Ladoy, P. (1993). Nonlinear variability of landscape topography: Multifractal analysis and simulation. In *Fractals in Geography* (Prentice Hall, p. 158-192). Nina Siu-Ngan Lam and Lee De Cola.

Loew, A., & Mauser, W. (2008). On the Disaggregation of Passive Microwave Soil Moisture Data Using *A Priori* Knowledge of Temporally Persistent Soil Moisture Fields. *IEEE Transactions on Geoscience and Remote Sensing*, *46*(3), 819-834. https://doi.org/10.1109/TGRS.2007.914800

Lovejoy, S., & Schertzer, D. (2008). Turbulence, raindrops and the $l^{1/2}$ number density law. *New Journal of Physics*, *10*(7), 075017. https://doi.org/10.1088/1367-2630/10/7/075017

Lovejoy, S., & Schertzer, D. (2010). Towards a new synthesis for atmospheric dynamics: Space–time cascades. *Atmospheric Research*, *96*(1), 1-52. https://doi.org/10.1016/j.atmosres.2010.01.004

Lovejoy, S., Tarquis, A. M., Gaonac'h, H., & Schertzer, D. (2008). Single-and multiscale remote sensing techniques, multifractals, and MODIS-derived vegetation and soil moisture. *Vadose Zone Journal*, *7*(2), 533–546. Consulté à l'adresse https://dl.sciencesocieties.org/publications/vzj/abstracts/7/2/533

Malbéteau, Y., Merlin, O., Gascoin, S., Gastellu, J. P., Mattar, C., Olivera-Guerra, L., Khabba, S., & Jarlan, L. (2017). Normalizing land surface temperature data for elevation and illumination effects in mountainous areas : A case study using ASTER data over a steep-sided valley in Morocco. *Remote Sensing of Environment*, *189*, 25-39. https://doi.org/10.1016/j.rse.2016.11.010

Malbéteau, Y., Merlin, O., Molero, B., Rüdiger, C., & Bacon, S. (2016). DisPATCh as a tool to evaluate coarse-scale remotely sensed soil moisture using localized in situ measurements: Application to SMOS and AMSR-E data in Southeastern Australia. *International Journal of Applied Earth Observation and Geoinformation*, *45*, 221-234. https://doi.org/10.1016/j.jag.2015.10.002

Manabe, S. (1969). CLIMATE AND THE OCEAN CIRCULATION [1]: I. THE ATMOSPHERIC CIRCULATION AND THE HYDROLOGY OF THE EARTH'S SURFACE. *Monthly Weather Review*, *97*(11), 739-774. https://doi.org/10.1175/1520-0493(1969)097<0739:CATOC>2.3.CO;2

Mandelbrot, B. (1967). How long is the coast of Britain? Statistical self-similarity and fractional dimension. S*cience*, *156*(3775), 636-638.

Mandelbrot, B. B. (1975). Stochastic models for the Earth's relief, the shape and the fractal dimension of the coastlines, and the number-area rule for islands. *Proceedings of the National Academy of Sciences*, *72*(10), 3825-3828. https://doi.org/10.1073/pnas.72.10.3825

Mandelbrot, B. B., & Van Ness, J. W. (1968). Fractional Brownian motions, fractional. *Geophys. Res. Lett*, *24*, 2099–2102. Consulté à l'adresse https://pdfs.semanticscholar.org/6a8f/dcdf9eaaf2145252f0a4ee6520ef2cf3f476.pdf

Manfreda, S., McCabe, M. F., Fiorentino, M., Rodríguez-Iturbe, I., & Wood, E. F. (2007). Scaling characteristics of spatial patterns of soil moisture from distributed modelling. *Advances in Water Resources*, *30*(10), 2145-2150. https://doi.org/10.1016/j.advwatres.2006.07.009

Mangiarotti, S., Le Jean, F., Huc, M. & Letellier, C. (2016). Global Modeling of aggregated and associated chaotic dynamics. *Chaos, Solitons & Fractals*, 83, 82-96.

Marshall, J. S., & Palmer, W. M. K. (1948). The distribution of raindrops with size. *Journal of meteorology*, *5*(4), 165-166.

Mascaro, G., & Vivoni, E. R. (2012). Comparison of Statistical and Multifractal Properties of Soil Moisture and Brightness Temperature From ESTAR and PSR During SGP99. *IEEE Geoscience and Remote Sensing Letters*, *9*(3), 373-377. https://doi.org/10.1109/LGRS.2011.2169770

Mascaro, G., Vivoni, E. R., & Deidda, R. (2010). Downscaling soil moisture in the southern Great Plains through a calibrated multifractal model for land surface modeling applications: DOWNSCALING SOIL MOISTURE IN THE GREAT PLAINS. *Water Resources Research*, *46*(8). https://doi.org/10.1029/2009WR008855

Merlin, O., Al Bitar, A., Walker, J. P., & Kerr, Y. (2010a). An improved algorithm for disaggregating microwave-derived soil moisture based on red, near-infrared and thermal-infrared data. *Remote Sensing of Environment*, *114*(10), 2305-2316. https://doi.org/10.1016/j.rse.2010.05.007

Merlin, O., Escorihuela, M. J., Mayoral, M. A., Hagolle, O., Al Bitar, A., & Kerr, Y. (2013). Self-calibrated evaporation-based disaggregation of SMOS soil moisture: An evaluation study at 3km and 100m resolution in Catalunya, Spain. *Remote Sensing of Environment*, *130*, 25-38. https://doi.org/10.1016/j.rse.2012.11.008

Merlin, O., Malbéteau, Y., Notfi, Y., Bacon, S., Khabba, S., & Jarlan, L. (2015). Performance Metrics for Soil Moisture Downscaling Methods: Application to DISPATCH Data in Central Morocco. *Remote Sensing*, *7*(4), 3783-3807. https://doi.org/10.3390/rs70403783

Merlin, O., Rudiger, C., Al Bitar, A., Richaume, P., Walker, J. P., & Kerr, Y. H. (2012). Disaggregation of SMOS Soil Moisture in Southeastern Australia. *IEEE Transactions on Geoscience and Remote Sensing*, *50*(5), 1556-1571. https://doi.org/10.1109/TGRS.2011.2175000

Merlin, O., Rüdiger, C., Richaume, P., Al Bitar, A., Mialon, A., Walker, J. P., & Kerr, Y. (2010b). Disaggregation as a top-down approach for evaluating 40 km resolution SMOS data using point-scale measurements: Application to AACES-1. In *Remote Sensing for Agriculture, Ecosystems, and Hydrology XII*(Vol. 7824, p. 78240I). International Society for Optics and Photonics. https://doi.org/10.1117/12.865751

Merlin, O., Stefan, V. G., Amazirh, A., Chanzy, A., Ceschia, E., Er-Raki, S., Gentine, P., Tallec, T., Ezzahar, J., Bircher, S., Beringer, J., & Khabba, S. (2016). Modeling soil evaporation efficiency in a range of soil and atmospheric conditions using a meta-analysis approach : MODELING SOIL EVAPORATION EFFICIENCY. *Water Resources Research*, *52*(5), 3663-3684. https://doi.org/10.1002/2015WR018233

Merlin, O., Walker, J., Chehbouni, A., & Kerr, Y. (2008a). Towards deterministic downscaling of SMOS soil moisture using MODIS derived soil evaporative efficiency. *Remote Sensing of Environment*, *112*(10), 3935-3946. https://doi.org/10.1016/j.rse.2008.06.012

Merlin, O., Walker, J. P., Kalma, J. D., Kim, E. J., Hacker, J., Panciera, R., Young, R., Summerell, G., Hornbuckle, J., Hafeez, M., & Jackson, T. (2008b). The NAFE'06 data set: Towards soil moisture retrieval at intermediate resolution. *Advances in Water Resources*, *31*(11), 1444-1455. https://doi.org/10.1016/j.advwatres.2008.01.018

Mohanty, B. ., & Skaggs, T. (2001). Spatio-temporal evolution and time-stable characteristics of soil moisture within remote sensing footprints with varying soil, slope, and vegetation. *Advances in Water Resources*, *24*(9-10), 1051-1067. https://doi.org/10.1016/S0309-1708(01)00034-3

Molero, B., Merlin, O., Malbéteau, Y., Al Bitar, A., Cabot, F., Stefan, V., Kerr, Y., Bacon, S., Cosh, M. H., Bindlish, R., & Jackson, T. J. (2016). SMOS disaggregated soil moisture product at 1 km resolution: Processor overview and first validation results. *Remote Sensing of Environment*, *180*, 361-376. https://doi.org/10.1016/j.rse.2016.02.045

Montzka, C., Jagdhuber, T., Horn, R., Bogena, H. R., Hajnsek, I., Reigber, A., & Vereecken, H. (2016). Investigation of SMAP Fusion Algorithms With Airborne Active and Passive L-Band Microwave Remote

Sensing. *IEEE Transactions on Geoscience and Remote Sensing*, *54*(7), 3878-3889. https://doi.org/10.1109/TGRS.2016.2529659

Moran, M. S., Clarke, T. R., Inoue, Y., & Vidal, A. (1994). Estimating crop water deficit using the relation between surface-air temperature and spectral vegetation index. *Remote Sensing of Environment*, *49*(3), 246-263. https://doi.org/10.1016/0034-4257(94)90020-5

Narayan, U., Lakshmi, V., & Jackson, T. J. (2006). High-resolution change estimation of soil moisture using L-band radiometer and Radar observations made during the SMEX02 experiments. *IEEE Transactions on Geoscience and Remote Sensing*, *44*(6), 1545-1554. https://doi.org/10.1109/TGRS.2006.871199

Njoku, E. G., Jackson, T. J., Lakshmi, V., Chan, T. K., & Nghiem, S. V. (2003). Soil moisture retrieval from AMSR-E. *IEEE Transactions on Geoscience and Remote Sensing*, *41*(2), 215-229. https://doi.org/10.1109/TGRS.2002.808243

Njoku, E. G., Wilson, W. J., Yueh, S. H., Dinardo, S. J., Li, F. K., Jackson, T. J., Lakshmi, V., & Bolten, J. (2002). Observations of soil moisture using a passive and active low-frequency microwave airborne sensor during SGP99. *IEEE Transactions on Geoscience and Remote Sensing*, *40*(12), 2659-2673. https://doi.org/10.1109/TGRS.2002.807008

Noilhan, J., & Planton, S. (1989). A simple parameterization of land surface processes for meteorological models. *Monthly weather review*, *117*(3), 536-549.

Oboukhov, A. M. (1962). Some specific features of atmospheric tubulence. *Journal of Fluid Mechanics*, *13*(01), 77. https://doi.org/10.1017/S0022112062000506

Ochsner, T. E., Cosh, M. H., Cuenca, R. H., Dorigo, W. A., Draper, C. S., Hagimoto, Y., Kerr, Y. H., Njoku, E. G., Small, E. E., & Zreda, M. (2013). State of the Art in Large-Scale Soil Moisture Monitoring. *Soil Science Society of America Journal*, *77*(6), 1888. https://doi.org/10.2136/sssaj2013.03.0093

Oldak, A., Pachepsky, Y., Jackson, T. J., & Rawls, W. J. (2002). Statistical properties of soil moisture images revisited. *Journal of Hydrology*, *255*(1-4), 12-24. https://doi.org/10.1016/S0022-1694(01)00507-8

Oliva, R., Daganzo, E., Kerr, Y. H., Mecklenburg, S., Nieto, S., Richaume, P., & Gruhier, C. (2012). SMOS Radio Frequency Interference Scenario: Status and Actions Taken to Improve the RFI Environment in the 1400–1427-MHz Passive Band. *IEEE Transactions on Geoscience and Remote Sensing*, *50*(5), 1427-1439. https://doi.org/10.1109/TGRS.2012.2182775

Owe, M., de Jeu, R., & Walker, J. (2001). A methodology for surface soil moisture and vegetation optical depth retrieval using the microwave polarization difference index. *IEEE Transactions on Geoscience and Remote Sensing*, *39*(8), 1643-1654. https://doi.org/10.1109/36.942542

Panciera, R., Walker, J. P., Jackson, T. J., Gray, D. A., Tanase, M. A., Ryu, D., Monerris, A., Yardley, H., Rudiger, C., Wu, X., Gao, Y., & Hacker, J. M. (2014). The Soil Moisture Active Passive Experiments (SMAPEx): Toward Soil Moisture Retrieval From the SMAP Mission. *IEEE Transactions on Geoscience and Remote Sensing*, *52*(1), 490-507. https://doi.org/10.1109/TGRS.2013.2241774

Parisi, G., & Frisch, U. (1985). A multifractal model of intermittency. In: Benzi, M., Parisi, R., Ghil, G. (Eds.), *Turbulence and Predictability in Geophysical Fluid Dynamics and Climate Dynamics*. Amsterdam, pp. 84–88.

Peischl, S., Walker, J. P., Rüdiger, C., Ye, N., Kerr, Y. H., Kim, E., Bandara, R., & Allahmoradi, M. (2012). The AACES field experiments: SMOS calibration and validation across the Murrumbidgee River catchment. *Hydrology and Earth System Sciences*, *16*(6), 1697-1708. https://doi.org/10.5194/hess-16-1697-2012

Pellenq, J., Kalma, J., Boulet, G., Saulnier, G.-M., Wooldridge, S., Kerr, Y., & Chehbouni, A. (2003). A disaggregation scheme for soil moisture based on topography and soil depth. *Journal of Hydrology*, *276*(1-4), 112-127. https://doi.org/10.1016/S0022-1694(03)00066-0

Peng, J., Loew, A., Merlin, O., & Verhoest, N. E. C. (2017). A review of spatial downscaling of satellite remotely sensed soil moisture: Downscale Satellite-Based Soil Moisture. *Reviews of Geophysics*, *55*(2), 341-366. https://doi.org/10.1002/2016RG000543

Peng, J., Loew, A., Zhang, S., Wang, J., & Niesel, J. (2016). Spatial Downscaling of Satellite Soil Moisture Data Using a Vegetation Temperature Condition Index. *IEEE Transactions on Geoscience and Remote Sensing*, *54*(1), 558-566. https://doi.org/10.1109/TGRS.2015.2462074

Petropoulos, G. P., Ireland, G., & Barrett, B. (2015). Surface soil moisture retrievals from remote sensing: Current status, products & future trends. *Physics and Chemistry of the Earth, Parts A/B/C*, *83-84*, 36-56. https://doi.org/10.1016/j.pce.2015.02.009

Piles, M., Camps, A., Vall-llossera, M., Corbella, I., Panciera, R., Rudiger, C., Kerr, Y., & Walker, J. (2011). Downscaling SMOS-Derived Soil Moisture Using MODIS Visible/Infrared Data. *IEEE Transactions on Geoscience and Remote Sensing*, *49*(9), 3156-3166. https://doi.org/10.1109/TGRS.2011.2120615

Piles, M., Entekhabi, D., & Camps, A. (2009). A Change Detection Algorithm for Retrieving High-Resolution Soil Moisture From SMAP Radar and Radiometer Observations. *IEEE Transactions on Geoscience and Remote Sensing*, *47*(12), 4125-4131. https://doi.org/10.1109/TGRS.2009.2022088

Rebora, N., Ferraris, L., Von Hardenberg, J., & Provenzale, A. (2006). Rainfall downscaling and flood forecasting : A case study in the Mediterranean area. *Natural Hazards and Earth System Science*, *6*(4), 611–619. Consulté à l'adresse https://hal.archives-ouvertes.fr/hal-00299348/

Richardson L.F. (1922). *Weather prediction by numerical process*, Cambridge Univ. Press.

Robinson, D. A., Campbell, C. S., Hopmans, J. W., Hornbuckle, B. K., Jones, S. B., Knight, R., Ogden, F., Selker, J., & Wendroth, O. (2008). Soil moisture measurement for ecological and hydrological watershed-scale observatories: A review. *Vadose Zone Journal*, *7*(1), 358-389.

Robock, A., Vinnikov, K. Y., Srinivasan, G., Entin, J. K., Hollinger, S. E., Speranskaya, N. A., Liu, S., Namkhai, A. (2000). The Global Soil Moisture Data Bank. *Bulletin of the American Meteorological Society*, *81*(6), 1281-1299. https://doi.org/10.1175/1520-0477(2000)081<1281:TGSMDB>2.3.CO;2

Rodriguez-Iturbe, I., Vogel, G. K., Rigon, R., Entekhabi, D., Castelli, F., & Rinaldo, A. (1995). On the spatial organization of soil moisture fields. *Geophysical Research Letters*, *22*(20), 2757-2760. https://doi.org/10.1029/95GL02779

Rötzer, K., Montzka, C., & Vereecken, H. (2015). Spatio-temporal variability of global soil moisture products. *Journal of Hydrology*, *522*, 187-202. https://doi.org/10.1016/j.jhydrol.2014.12.038

Ryu, D., & Famiglietti, J. S. (2006). Multi-scale spatial correlation and scaling behavior of surface soil moisture. *Geophysical Research Letters*, *33*(8), L08404. https://doi.org/10.1029/2006GL025831

Schertzer, D., & Lovejoy, S. (1984). On the dimension of atmospheric motions. *Turbulence and Chaotic phenomena in Fluids*, 505-512.

Schertzer, D., & Lovejoy, S. (1987). Physical modeling and analysis of rain and clouds by anisotropic scaling multiplicative processes. *Journal of Geophysical Research*, *92*(D8), 9693. https://doi.org/10.1029/JD092iD08p09693

Schertzer, D., & Lovejoy, S. (1991). Nonlinear geodynamical variability: multiple singularities, universality and observables. In *Non-Linear Variability in Geophysics* (pp. 41-82). Springer, Dordrecht.

Schertzer, D., & Lovejoy, S. (1997). Universal multifractals do exist!: Comments on "A statistical analysis of mesoscale rainfall as a random cascade". *Journal of Applied Meteorology*, *36*(9), 1296–1303.

Schmitt, F. (1993). Estimation of universal multifractal indices for atmospheric turbulent velocity fileds. *Fractals*, *1*(3), 568-575.

Sharma, D. (2007). Spatial disaggregation of bias-corrected GCM precipitation for improved hydrologic simulation : Ping River Basin, Thailand. *Hydrol. Earth Syst. Sci.*, 19.

She, Z.-S., & Leveque, E. (1994). Universal Scaling Laws in Fully Developed Turbulence. *Physical review letters*, *72*(3).

Si, B. C. (2008). Spatial scaling analyses of soil physical properties: A review of spectral and wavelet methods. *Vadose Zone Journal*, *7*(2), 547-562.

Smith, A. B., Walker, J. P., Western, A. W., Young, R. I., Ellett, K. M., Pipunic, R. C., Grayson, R. B., Siriwardena, L., Chiew, F. H. S., & Richter, H. (2012). The Murrumbidgee soil moisture monitoring network data set: DATA AND ANALYSIS NOTE. *Water Resources Research*, *48*(7). https://doi.org/10.1029/2012WR011976

Sohrabinia, Find pixel indices in HDF-EOS files based on LatLon coordinates, https://fr.mathworks.com/matlabcentral/fileexchange/37033-find-pixel-indices-in-hdf-eos-files-based-on-latlon-coordinates, (15 June 2012).

Solano, R., Didan, K., Jacobson, A., & Huete, A. (2010). MODIS vegetation index user's guide (MOD13 series). *Vegetation Index and Phenology Lab, The University of Arizona*, 1-38.

Song, C., Jia, L., & Menenti, M. (2014). Retrieving High-Resolution Surface Soil Moisture by Downscaling AMSR-E Brightness Temperature Using MODIS LST and NDVI Data. *IEEE Journal of Selected Topics in Applied Earth Observations and Remote Sensing*, *7*(3), 935-942. https://doi.org/10.1109/JSTARS.2013.2272053

Tessier, Y., Lovejoy, S., & Schertzer, D. (1993). Universal Multifractals: Theory and Observations for Rain and Clouds. https://doi.org/10.1175/1520-0450

Vereecken, H., Huisman, J. A., Pachepsky, Y., Montzka, C., van der Kruk, J., Bogena, H., Weihermüller , L., Herbst, M., Martinez, G., & Vanderborght, J. (2014). On the spatio-temporal dynamics of soil moisture at the field scale. *Journal of Hydrology*, *516*, 76-96. https://doi.org/10.1016/j.jhydrol.2013.11.061

Verhoest, N. E. C., van den Berg, M. J., Martens, B., Lievens, H., Wood, E. F., Pan, M., Wood, E. F., Pan, M., Kerr, Y. H., Al Bitar, A., Tomer, S. K., Drusch, M., Vernieuwe, H., De Baets, B., Walker, J. P., Dumedah, G., & Pauwels, V. R. N. (2015). Copula-Based Downscaling of Coarse-Scale Soil Moisture Observations With

Implicit Bias Correction. *IEEE Transactions on Geoscience and Remote Sensing*, *53*(6), 3507-3521. https://doi.org/10.1109/TGRS.2014.2378913

Verrier, S., Barthès, L., & Mallet, C. (2013). Theoretical and empirical scale dependency of Z-R relationships : Evidence, impacts, and correction: SCALE DEPENDENCY OF Z-R RELATIONSHIPS. *Journal of Geophysical Research: Atmospheres*, *118*(14), 7435-7449. https://doi.org/10.1002/jgrd.50557

Verrier, S., de Montera, L., Barthès, L., & Mallet, C. (2010). Multifractal analysis of African monsoon rain fields, taking into account the zero rain-rate problem. *Journal of Hydrology*, *389*(1-2), 111-120. https://doi.org/10.1016/j.jhydrol.2010.05.035

Verrier, S., Mallet, C., & Barthès, L. (2011). Multiscaling properties of rain in the time domain, taking into account rain support biases. *Journal of Geophysical Research*, *116*(D20). https://doi.org/10.1029/2011JD015719

Wagner, W., Sabel, D., Doubkova, M., Bartsch, A., & Pathe, C. (2009). THE POTENTIAL OF SENTINEL-1 FOR MONITORING SOIL MOISTURE WITH A HIGH SPATIAL RESOLUTION AT GLOBAL SCALE, 5.

Walker, J. P., & Houser, P. R. (2004). Requirements of a global near-surface soil moisture satellite mission: accuracy, repeat time, and spatial resolution. *Advances in Water Resources*, *27*(8), 785-801. https://doi.org/10.1016/j.advwatres.2004.05.006

Wan, Z. (2006). MODIS Land Surface Temperature Products Users' Guide - Collection 5. South Dakota: Sioux Falls (Retrieved from http://www.icess.ucsb.edu/modis/LstUsrGuide/MODIS_LST_products_Users_guide_C5.pdf).

Werbylo, K. L., & Niemann, J. D. (2014). Evaluation of sampling techniques to characterize topographically-dependent variability for soil moisture downscaling. *Journal of Hydrology*, *516*, 304-316. https://doi.org/10.1016/j.jhydrol.2014.01.030

Western, A. W., Zhou, S.-L., Grayson, R. B., McMahon, T. A., Blöschl, G., & Wilson, D. J. (2004). Spatial correlation of soil moisture in small catchments and its relationship to dominant spatial hydrological processes. *Journal of Hydrology*, *286*(1-4), 113-134. https://doi.org/10.1016/j.jhydrol.2003.09.014

Wigneron, J.-P., Calvet, J.-C., Pellarin, T., Van de Griend, A. ., Berger, M., & Ferrazzoli, P. (2003). Retrieving near-surface soil moisture from microwave radiometric observations: current status and future plans. *Remote Sensing of Environment*, *85*(4), 489-506. https://doi.org/10.1016/S0034-4257(03)00051-8

Wigneron, J.-P., Kerr, Y., Waldteufel, P., Saleh, K., Escorihuela, M.-J., Richaume, P., Ferrazzoli, P., de Rosnay, P., Gurney, R., Calvet, J.-C., Grant, J. P., Guglielmetti, M., Hornbuckle, B., Matzler, C., Pellarin, T., Schwank, M. & Schwank, M. (2007). L-band Microwave Emission of the Biosphere (L-MEB) Model: Description and calibration against experimental data sets over crop fields. *Remote Sensing of Environment*, *107*(4), 639-655. https://doi.org/10.1016/j.rse.2006.10.014

Xiwu Zhan, Houser, P. R., Walker, J. P., & Crow, W. T. (2006). A method for retrieving high-resolution surface soil moisture from hydros L-band radiometer and Radar observations. *IEEE Transactions on Geoscience and Remote Sensing*, *44*(6), 1534-1544. https://doi.org/10.1109/TGRS.2005.863319

Yaglom, A. M. (1966). The influence of fluctuations in energy dissipation on the shape of turbulence characteristics in the inertial interval. In *Soviet Physics Doklady* (Vol. 11, p. 26).

Zhan, X., Miller, S., Chauhan, N., Di, L., & Ardanuy, P. (2002). Soil moisture visible/infrared radiometer suite algorithm theoretical basis document. *Raytheon Syst. Company, Lanham, MD*.

Zhao, W., & Li, A. (2013). A Downscaling Method for Improving the Spatial Resolution of AMSR-E Derived Soil Moisture Product Based on MSG-SEVIRI Data. *Remote Sensing*, *5*(12), 6790-6811. https://doi.org/10.3390/rs5126790